Detectability of the gravitational redshift effect from the asymmetric galaxy clustering

Shohei Saga, Atsushi Taruya, Yann Rasera, Michel-Andrès Breton

Monthly Notices of the ROYAL ASTRONOMICAL SOCIETY

MNRAS **511,** 2732–2754 (2022) https://doi.org/10.1093/mnras/stac186
Advance Access publication 2022 January 28

Detectability of the gravitational redshift effect from the asymmetric galaxy clustering

Shohei Saga [1]★ Atsushi Taruya [2,3] Yann Rasera[4] and Michel-Andrès Breton[5]

[1]*Laboratoire Univers et Théories, Observatoire de Paris, Université PSL, Université de Paris, CNRS, F-92190 Meudon, France*
[2]*Center for Gravitational Physics, Yukawa Institute for Theoretical Physics, Kyoto University, Kyoto 606-8502, Japan*
[3]*Kavli Institute for the Physics and Mathematics of the Universe (WPI), The University of Tokyo Institutes for Advanced Study, The University of Tokyo, 5-1-5 Kashiwanoha, Kashiwa, Chiba 277-8583, Japan*
[4]*Laboratoire Univers et Théories, Université de Paris, Observatoire de Paris, Université PSL, CNRS, F-92190 Meudon, France*
[5]*Aix Marseille Univ, CNRS, CNES, LAM, Marseille, F-13013, France*

Accepted 2022 January 18. Received 2021 December 18; in original form 2021 September 20

ABSTRACT

It has been recently recognized that the observational relativistic effects, mainly arising from the light propagation in an inhomogeneous universe, induce the dipole asymmetry in the cross-correlation function of galaxies. In particular, the dipole asymmetry at small scales is shown to be dominated by the gravitational redshift effects. In this paper, we exploit a simple analytical description for the dipole asymmetry in the cross-correlation function valid at quasi-linear regime. In contrast to the previous model, a new prescription involves only 1D integrals, providing a faster way to reproduce the results obtained by Saga et al. Using the analytical model, we discuss the detectability of the dipole signal induced by the gravitational redshift effect from upcoming galaxy surveys. The gravitational redshift effect at small scales enhances the signal-to-noise ratio (S/N) of the dipole, and in most of the cases considered, the S/N is found to reach a maximum at $z \approx 0.5$. We show that current and future surveys such as DESI and SKA provide an idealistic data set, giving a large S/N of 10–20. Two potential systematics arising from off-centred galaxies are also discussed (transverse Doppler effect and diminution of the gravitational redshift effect), and their impacts are found to be mitigated by a partial cancellation between two competitive effects. Thus, the detection of the dipole signal at small scales is directly linked to the gravitational redshift effect, and should provide an alternative route to test gravity.

Key words: gravitation – cosmology: theory – large-scale structure of Universe.

1 INTRODUCTION

Mapping the large-scale structure of the universe with galaxy surveys is currently a major science driver for cosmology. In particular, through its statistical characterizations such as two-point correlation function or power spectrum, the large-scale galaxy distribution enables us to probe the late-time cosmic expansion, growth of structure, and even the primordial fluctuations. However, the observed 3D map of galaxies does not directly reflect the true galaxy distribution because of a number of physical effects. The most prominent effect is the Doppler effect induced by the peculiar velocities of galaxies, which produces apparent anisotropies along the line-of-sight direction, known as redshift-space distortions (RSD) (Kaiser 1987; Hamilton 1992). The RSD has now been recognized as a sensitive probe of the growth of cosmic structure, and the measurement of it provides a unique opportunity for a test of gravity on cosmological scales (e.g. Guzzo et al. 2008; Linder 2008; Percival & White 2009; Reid et al. 2012; Sánchez et al. 2013; Alam et al. 2017a). The upcoming galaxy surveys will observe an unprecedented number of galaxies and provide us with high-precision measurements of RSD, which can further offer a way to detect small but non-negligible special and general relativistic contributions to RSD (Sasaki 1987; Pyne & Birkinshaw 2004; Yoo, Fitzpatrick & Zaldarriaga 2009; Yoo 2010; Bonvin & Durrer 2011; Challinor & Lewis 2011; Yoo 2014).

Recently, it has been shown that relativistic effects arising from the light propagation in an inhomogeneous universe, e.g. gravitational redshift, integrated Sachs-Wolfe, and weak lensing effects, produce asymmetric distortions to the galaxy distribution along the line-of-sight direction (Yoo et al. 2012; Croft 2013; Tansella et al. 2018). This means that with a certain line-of-sight definition, applying the multipole expansion to the cross-correlation function or power spectrum between different biased objects yields non-vanishing odd multipole moments, with the largest signals coming from the dipole moment (e.g. McDonald 2009; Bonvin, Hui & Gaztañaga 2014). Detection of such relativistic signals would provide a new window to probe gravity on cosmological scales, thus complementary to the measurement of the redshift-space distortions induced by the Doppler effect. Further, it can offer a fundamental or classical test of gravity from a viewpoint of the equivalence principle, helpful to constrain cosmology (e.g. Bonvin & Fleury 2018; Bonvin, Oliveira Franco & Fleury 2020). Recently, Alam et al. (2017b) have claimed the detection of the asymmetry at the 2.8σ level using SDSS BOSS DR12 CMASS galaxy sample. Their results are consistent with the gravita-

★ E-mail: shohei.saga@obspm.fr

tional redshift effect predicted by general relativity (see also Wojtak, Hansen & Hjorth 2011; Jimeno et al. 2015; Sadeh, Feng & Lahav 2015; Mpetha et al. 2021, for the detection using clusters of galaxies).

In our previous studies, toward a solid detection of the non-vanishing relativistic dipole in the cross-correlation function, we have numerically constructed halo catalogues on light cone, taking consistently the observational relativistic effects into account (Breton et al. 2019) (see Borzyszkowski, Bertacca & Porciani 2017; Coates et al. 2020; Guandalin et al. 2021, for recent similar works at lower resolution). At large scales, we found that the standard Doppler effect without taking the distant-observer approximation gives the largest contribution to the dipole (Taruya et al. 2020). On the other hand, at the scales beyond the linear regime, the gravitational redshift effect starts to dominate the dipole, and the linear theory prediction fails to reproduce the simulation results.

In order to quantitatively explain major findings in the numerical simulations, Saga et al. (2020) developed a quasi-linear model based on the Zel'dovich approximation. The model considers the standard Doppler and gravitational redshift effects as dominant relativistic contributions, taking also the so-called wide-angle effect of RSD into account in a self-consistent way. In particular, the model accounts for the non-perturbative contribution to the gravitational redshift effect arising from the halo potential, which is shown to play an important role to describe the small-scale behaviours of the dipole moment, leading to a remarkable agreement with the dipole cross-correlations measured in simulations at quasi-linear scales ($s \gtrsim 5\,\mathrm{Mpc}\,h^{-1}$).

In this paper, based on the success of our numerical and analytical modelling, we pursue to further investigate the relativistic dipole, focusing specifically on its future detectability. Several authors have investigated the feasibility to detect the relativistic dipole, but they rely on the linear theory prediction, and consider large scales (Hall & Bonvin 2017; Lepori et al. 2018). Contrary to these previous works, our study here is based on a model capable of going beyond linear regime, taking the non-linear gravitational potential of haloes into account. A similar study focusing on small scales has been recently done by Beutler & Di Dio (2020), using the third-order Eulerian perturbation theory. They considered the power spectrum dipole, i.e. the Fourier counterpart of the dipole cross-correlation function, and dividing a single galaxy population observed by Dark Energy Spectroscopic Instrument[1] (DESI; DESI Collaboration 2016) into more than two subsamples, they found that the signal-to-noise ratio of their cross power spectrum exceeds 10 if the difference of the (linear) galaxy biases between two subsamples, Δb, becomes $\Delta b = 1$. In this paper, we estimate the signal-to-noise ratio for the cross-correlation function, and applying the multitracer techniques, we discuss systematically the detectability of the relativistic dipole through the combination of various upcoming galaxy surveys. In doing so, we will first present a simple analytical model, which quantitatively reproduces major trends obtained from our previous study (Saga et al. 2020). In contrast to our previous model which involves seven dimensional integrals, the prediction of the dipole in the present model needs only the 1D integrals, hence providing a faster way to estimate the signal-to-noise ratio. We will then examine the detectability of relativistic dipole in various upcoming surveys: DESI (DESI Collaboration 2016), *Euclid*[2] (Laureijs et al. 2011), Subaru Prime Focus Spectrograph[3] (PFS; Takada et al. 2014), and Square Kilometre Array[4] (SKA; Square Kilometre Array Cosmology Science Working Group 2020). Moreover, potentially important systematics are also investigated, and incorporating these effects into the analytical model, we quantitatively predict their impacts on the dipole cross-correlation function.

This paper is organized as follows. In Section 2, we present a simple analytical model for the relativistic dipole induced by the Doppler and gravitational redshift effects, which involves only 1D integrals. In Section 3, we write down the estimator for the dipole moment of the cross-correlation function and compute its covariance matrix following Bonvin, Hui & Gaztanaga (2016), Hall & Bonvin (2017). This is used in Section 4 to estimate the signal-to-noise ratio of the dipole moment for various upcoming surveys. In Section 5, we discuss a potential impact of the systematic effects from off-centred galaxies on the dipole moment. Finally, Section 6 is devoted to the summary of important findings.

Supplementing with the analysis and results in the main text, Appendices A, B, and C provide, respectively, key expressions to derive the analytical expression for the dipole cross-correlation function in our simple model, the comparison of its model with an approximate description discussed in our previous paper, and the analytical expressions of the non-vanishing multipoles based on the model. Appendix D discusses the impact of the effect ignored in our analytical model on the dipole signal, particularly focusing on the Doppler magnification. In Appendix E, we summarize the parameters characterizing upcoming galaxy surveys, which are used to estimate the signal-to-noise ratio of the dipole in Section 4. In Appendix F, we present an alternative way to estimate the signal-to-noise ratio, in which the halo subsamples to cross-correlate are characterized by the minimum halo mass and the width of (logarithmic) halo mass bins.

Throughout this paper, we assume a flat Lambda cold dark matter (ΛCDM) model. The fiducial values of cosmological parameters are chosen so as to match the numerical simulations (Borzyszkowski et al. 2017), based on the seven-year *WMAP* results (Komatsu et al. 2011): $\Omega_{\mathrm{m0}} = 0.25733$, $\Omega_{\mathrm{b0}} = 0.04356$, $\Omega_{\Lambda 0} = 0.74259$, and $\Omega_{\mathrm{r0}} = 8.076 \times 10^{-5}$ for the density parameters for matter, baryon, dark energy with equation-of-state parameter $w = -1$, and radiation, respectively, at the present time. The other cosmological parameters are chosen as $h = 0.72$, $n_{\mathrm{s}} = 0.963$, and $\sigma_8 = 0.801$ for the Hubble parameter, scalar spectral index, and the root-mean-square matter density fluctuations with a top-hat filter of radius $8\,h^{-1}$ Mpc. Throughout the paper, we will work with units of $c = 1$.

2 MODEL

The main purpose of this paper is to quantitatively estimate the detectability of the relativistic dipole, arising from the gravitational redshift effects, in upcoming deep and wide surveys. In doing so, we first present an analytical model of dipole cross-correlation function in this section. The model presented below involves only 1D integrals, and hence it provides a fast way to predict the relativistic dipole as well as to estimate its signal-to-noise ratio based on the covariance matrix calculations.

In modelling the dipole cross-correlation function, the standard Doppler effect has to be also taken into account, since it gives a dominant contribution to the dipole at large scales through the so-called wide-angle effect (Fisher, Scharf & Lahav 1994; Hamilton & Culhane 1996; Zaroubi & Hoffman 1996; Szalay, Matsubara & Landy 1998; Matsubara 2000; Matsubara 2004; Szapudi 2004;

[1] https://www.desi.lbl.gov/
[2] https://www.euclid-ec.org/
[3] http://sumire.ipmu.jp/en/
[4] https://www.skatelescope.org/

Pápai & Szapudi 2008). Considering both the Doppler and gravitational redshift effects, Saga et al. (2020) constructed a quasi-linear model based on the Zel'dovich approximation. To account for the non-perturbative contributions at small scales, we combined it with the halo model to predict the relativistic dipole from the halo potential. In Section 2.1, starting from the expression in our previous work, we derive a simplified expression for the density field by linearizing the displacement fields but still retaining the non-perturbative contribution. Then, the expression for the dipole cross-correlation function is simplified, and is presented in Section 2.2.

2.1 Modelling observed density fields

Consider an object at the true position $\boldsymbol{x}$ in comoving space. In redshift space, the observed position $\boldsymbol{s}$ generally differs from $\boldsymbol{x}$, mainly due to the standard Doppler effect. Taking also into account the relativistic corrections, which we denote by ϵ, the relation between the two positions $\boldsymbol{x}$ and $\boldsymbol{s}$ is given by (e.g. Challinor & Lewis 2011):

$$\boldsymbol{s} = \boldsymbol{x} + \frac{1}{aH}(\boldsymbol{v}\cdot\hat{\boldsymbol{x}})\hat{\boldsymbol{x}} + \epsilon(\boldsymbol{x})\hat{\boldsymbol{x}}, \tag{1}$$

where $\hat{\boldsymbol{x}}$ is the unit vector defined by $\hat{\boldsymbol{x}} = \boldsymbol{x}/|\boldsymbol{x}|$ and a, H, and $\boldsymbol{v}$ are a scale factor, Hubble parameter, and peculiar velocity of the object, respectively. Note that the expression at equation (1) is valid in the weak-field approximation of metric perturbation, and $|\boldsymbol{v}| \ll 1$. In equation (1), we also ignore the gravitational lensing effect, which has been shown to give a very minor contribution to the asymmetric cross-correlation, i.e. odd multipole anisotropies. The term ϵ includes the contributions of gravitational redshift, integrated Sachs-Wolfe, transverse Doppler, and Shapiro time-delay effects, among which the gravitational redshift effect gives the most dominant relativistic contribution. Thus, focusing on the major relativistic effect, it is expressed as

$$\epsilon(\boldsymbol{x}) = -\frac{1}{aH}\phi(\boldsymbol{x}), \tag{2}$$

where the function $\phi(\boldsymbol{x})$ stands for the gravitational potential. The explicit forms of other relativistic contributions to the observed source position can be found in the literature (e.g. Yoo 2010; Bonvin & Durrer 2011; Challinor & Lewis 2011).

To derive a simplified expression for the correlation function, we first follow the analytical treatment given by Saga et al. (2020), who applied the Zel'dovich approximation to predict the cross-correlation function beyond linear regime (Novikov 1969; Zel'dovich 1970; Shandarin & Zeldovich 1989). The Zel'dovich approximation, known as the first-order Lagrangian perturbation theory, describes the motion of mass element at the Eulerian position $\boldsymbol{x}$, introducing the Lagrangian displacement field, $\boldsymbol{\Psi}$, which is given as a function of the Lagrangian position (initial position) $\boldsymbol{q}$. Assuming that the objects of our interest follow the velocity flow of mass distributions, the Eulerian position, and the velocity of each mass element at $\boldsymbol{x}$, $\boldsymbol{v}$, at a given time t are generally expressed as

$$\boldsymbol{x}(\boldsymbol{q}, t) = \boldsymbol{q} + \boldsymbol{\Psi}(\boldsymbol{q}, t), \tag{3}$$

$$\boldsymbol{v}(\boldsymbol{x}) = a\frac{\mathrm{d}\boldsymbol{\Psi}}{\mathrm{d}t}. \tag{4}$$

The displacement field should satisfy the condition $\boldsymbol{\Psi} \to 0$ at $t \to 0$. In the Zel'dovich approximation, it is expressed in terms of the (Lagrangian) linear density field $\delta_{\rm L}$ as $\boldsymbol{\nabla}_q \cdot \boldsymbol{\Psi}_{\rm ZA} = -\delta_{\rm L}$, with the operator $\boldsymbol{\nabla}_q$ being a spatial derivative with respect to the Lagrangian coordinate. Recalling that the linear density field is related to initial density field δ_0 through $\delta_{\rm L} = D_+(t)\delta_0$ with D_+ being the linear growth factor, the velocity field is rewritten with

$$\boldsymbol{v} = aHf\boldsymbol{\Psi}_{\rm ZA}, \tag{5}$$

where the quantity f is the linear growth rate defined by $f \equiv \mathrm{d}\ln D_+(a)/\mathrm{d}\ln a$.

Substituting the expressions at equations (3) and (5) into equation (1), the relation between the redshift-space position $\boldsymbol{s}$ and the Lagrangian-space position $\boldsymbol{q}$ becomes

$$\begin{aligned} s_i &= q_i + \{\delta_{ij} + f\,\hat{x}_i\hat{x}_j\}\Psi_i(\boldsymbol{q}) + \epsilon(\boldsymbol{x})\hat{x}_i \\ &\simeq q_i + R_{ij}(\hat{\boldsymbol{q}})\Psi_j(\boldsymbol{q}) + \epsilon(\boldsymbol{q})\hat{q}_i, \end{aligned} \tag{6}$$

with the matrix R_{ij} defined by $R_{ij}(\hat{\boldsymbol{q}}) \equiv \delta_{ij} + f\hat{q}_i\hat{q}_j$. Here, we used the Einstein summation convention and omit the subscript ZA, simply writing $\boldsymbol{\Psi}_{\rm ZA}$ as $\boldsymbol{\Psi}$. Note that the second line is valid at first-order displacement field (i.e. Zel'dovich approximation).

Given the relation at equation (6), the number density field of the object in redshift space, $n^{(\rm S)}$, is expressed in terms of the quantities defined in Lagrangian space. We have

$$n^{(\rm S)}(\boldsymbol{s})\mathrm{d}^3\boldsymbol{s} = \overline{n}\left(1 + b^{\rm L}\delta_{\rm L}(\boldsymbol{q})\right)\mathrm{d}^3\boldsymbol{q}, \tag{7}$$

where the quantity $b^{\rm L}$ is the Lagrangian linear bias parameter, and $\overline{n}$ is the mean number density at a given redshift. The above expression is recast as

$$\begin{aligned} n^{(\rm S)}(\boldsymbol{s}) &= \overline{n}\left(1 + b^{\rm L}\delta_{\rm L}(\boldsymbol{q})\right)\left|\frac{\partial s_i}{\partial q_j}\right|^{-1} \\ &= \overline{n}\int \mathrm{d}^3\boldsymbol{q}\ \left(1 + b^{\rm L}\delta_{\rm L}(\boldsymbol{q})\right)\delta_{\rm D}(s_i - q_i - R_{ij}\Psi_j + \epsilon\hat{q}_i) \\ &= \overline{n}\int \mathrm{d}^3\boldsymbol{q}\ \int \frac{\mathrm{d}^3\boldsymbol{k}}{(2\pi)^3}\,\mathrm{e}^{\mathrm{i}k_i\left(s_i - q_i - R_{ij}\Psi_j - \epsilon\hat{q}_i\right)}\left(1 + b^{\rm L}\delta_{\rm L}(\boldsymbol{q})\right). \end{aligned} \tag{8}$$

Let us now consider the density fluctuation. Denoting it by $\delta^{(\rm S)}$, we define

$$\delta^{(\rm S)}(\boldsymbol{s}) = \frac{n^{(\rm S)}(\boldsymbol{s})}{\left\langle n^{(\rm S)}(\boldsymbol{s})\right\rangle} - 1, \tag{9}$$

where the bracket $\langle\cdots\rangle$ stands for the ensemble average. Here, it is to be noted that the quantity $\langle n^{(\rm S)}\rangle$ generally differs from $\overline{n}$, due to the directional-dependent matrix R_{ij} and relativistic correction along the line-of-sight direction. In the presence of these terms, a naive substitution of equation (8) into the above yields an intricate expression for the correlation function which involves the multidimensional integrals in both numerator and denominator. Indeed, without invoking any approximation, Saga et al. (2020) derived an exact expression for the cross-correlation function from equation (9) (see also Taruya et al. 2020), with which the prediction of the dipole moment is made numerically by performing seven dimensional integrals, requiring a time-consuming computation. However, ignoring the relativistic contribution, a detailed comparison of the predictions between the exact expression and the linear theory has shown that the results almost coincide with each other (Taruya et al. 2020). One can thus linearize the expression at (9) with respect to the displacement field. Further, the relativistic corrections, which are supposed to be small, can be also expanded from the exponent. Then, we obtain

$$\begin{aligned} \delta^{(\rm S)}(\boldsymbol{s}) = \int \mathrm{d}^3\boldsymbol{q}\ \int \frac{\mathrm{d}^3\boldsymbol{k}}{(2\pi)^3}\,\mathrm{e}^{\mathrm{i}\boldsymbol{k}\cdot(\boldsymbol{s}-\boldsymbol{q})}\Big[&-(\epsilon - \langle\epsilon\rangle)\,\mathrm{i}\boldsymbol{k}\cdot\hat{\boldsymbol{q}} \\ &+ \left(1 - \epsilon(\mathrm{i}\boldsymbol{k}\cdot\hat{\boldsymbol{q}}) + 2\frac{\langle\epsilon\rangle}{s}\right)\left(b^{\rm L}\delta_{\rm L} - \mathrm{i}k_i R_{ij}\Psi_j\right)\Big]. \end{aligned} \tag{10}$$

Here, in computing the density field for galaxies/haloes, we have to be careful of dealing with the term ϵ coming from the gravitational redshift effect. Although the term ϵ itself should be a small quantity, the gravitational potential at the halo/galaxy position would not be simply characterized by the gravitational potential of the linear density field. Since the haloes/galaxies are likely to be formed in the presence of a deep potential well through non-linear processes, it should involve the non-perturbative contribution. Thus, following Saga et al. (2020), we decompose the gravitational redshift contribution ϵ into two pieces:

$$\epsilon(\boldsymbol{x}) = \epsilon_{\rm L}(\boldsymbol{x}) + \epsilon_{\rm NL}. \tag{11}$$

In equation (11), the first term at the right-hand side, $\epsilon_{\rm L}(\boldsymbol{x})$, represents the linear-order contribution arising from the gravitational potential of the linear density field, $\phi_{\rm L}$:

$$\epsilon_{\rm L}(\boldsymbol{x}) = -\frac{1}{aH}\phi_{\rm L}(\boldsymbol{x}). \tag{12}$$

On the other hand, the second term, $\epsilon_{\rm NL}$ describes the non-perturbative contribution. In this paper, we shall model it with the universal halo density profile called NFW profile by Navarro, Frenk & White (1996), as adopted in Saga et al. (2020):

$$\epsilon_{\rm NL} = -\frac{1}{aH}\phi_{\rm NFW,0}(z, M) \tag{13}$$

with $\phi_{\rm NFW,0}$ being the halo potential of the NFW profile at the centre (see Appendix D in Saga et al. 2020 for the explicit form of the NFW potential $\phi_{\rm NFW,0}$). Here, we assume that the object to cross-correlate resides at the halo centre. The potential impact of this assumption will be later discussed in Section 5. Note that the non-perturbative potential contribution, $\epsilon_{\rm NL}$, is not a random variable but a constant value as a function of the halo mass and redshift through equation (13). Thus, we have $\langle\epsilon\rangle = \epsilon_{\rm NL}$.

Keeping the above points in mind, we substitute equations (11) and (12) into equation (10). After performing the integration by parts, the density fluctuation $\delta^{\rm (S)}$ is recast in the following form:

$$\delta^{\rm (S)}(\boldsymbol{s}) = \delta^{\rm (std)}(\boldsymbol{s}) + \delta^{\rm (pot)}(\boldsymbol{s}) + \delta^{(\epsilon_{\rm NL})}(\boldsymbol{s}). \tag{14}$$

Here, we classify the density fluctuations into three contributions: the standard Doppler effects without assuming the plane-parallel limit, $\delta^{\rm (std)}(\boldsymbol{s})$, the gravitational redshift effect due to the linear density fields, $\delta^{\rm (pot)}(\boldsymbol{s})$, and gravitational redshift effect due to the non-linear halo potential, $\delta^{(\epsilon_{\rm NL})}(\boldsymbol{s})$. Those contributions are explicitly given by

$$\delta^{\rm (std)}(\boldsymbol{s}) \equiv \int \frac{{\rm d}^3\boldsymbol{k}}{(2\pi)^3} {\rm e}^{{\rm i}\boldsymbol{k}\cdot\boldsymbol{s}} \left[b + f\mu_k^2 - {\rm i}f\frac{2}{ks}\mu_k\right]\delta_{\rm L}(\boldsymbol{k}), \tag{15}$$

$$\delta^{\rm (pot)}(\boldsymbol{s}) \equiv \int \frac{{\rm d}^3\boldsymbol{k}}{(2\pi)^3} {\rm e}^{{\rm i}\boldsymbol{k}\cdot\boldsymbol{s}} \left[({\rm i}ks\mu_k + 2)\frac{\mathcal{M}}{sk^2}\right]\delta_{\rm L}(\boldsymbol{k}), \tag{16}$$

$$\delta^{(\epsilon_{\rm NL})}(\boldsymbol{s}) \equiv \frac{\epsilon_{\rm NL}}{s}\int \frac{{\rm d}^3\boldsymbol{k}}{(2\pi)^3} {\rm e}^{{\rm i}\boldsymbol{k}\cdot\boldsymbol{s}} \left[-1 + \mu_k^2 - {\rm i}f\frac{2}{ks}\mu_k - {\rm i}bks\mu_k - 2f\mu_k^2 - {\rm i}\frac{2}{ks}\mu_k - {\rm i}fks\mu_k^3\right]\delta_{\rm L}(\boldsymbol{k}), \tag{17}$$

with the quantity μ being the directional cosine defined by $\mu_k \equiv \hat{\boldsymbol{s}}\cdot\hat{\boldsymbol{k}}$. Here, we introduced a new quantity $\mathcal{M} \equiv -3\Omega_{\rm m0}H_0^2/(2a^2H)$. The quantity b is the Eulerian linear bias parameter, which is related to the Lagrangian linear bias $b^{\rm L}$ through $b = 1 + b^{\rm L}$. Note that in the above, the gravitational potential $\phi_{\rm L}$ is rewritten with the linear density fields through the Poisson equation. The linear-order contributions given in equations (15) and (16) reproduce the results obtained previously if one neglects other minor contributions but keep the terms at the $O(aH/k)$ order (see e.g. equation (A7) in Bonvin et al. (2014) or equation (1) in Hall & Bonvin (2017)).

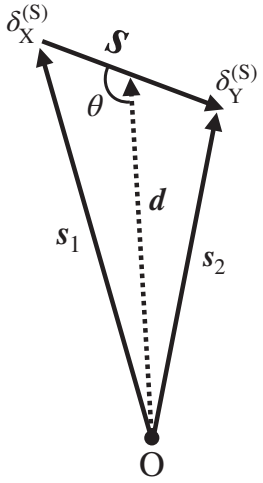

Figure 1. The geometric configuration of the cross-correlation function in redshift space. The biased objects $\delta_{\rm X}^{\rm (S)}$ and $\delta_{\rm Y}^{\rm (S)}$ are, respectively, observed at $\boldsymbol{s}_1$ and $\boldsymbol{s}_2$ with respect to the observer (O). Here we assume $b_{\rm X} > b_{\rm Y}$. The separation vector, line-of-sight vector, and directional cosine are defined by $\boldsymbol{s} = \boldsymbol{s}_2 - \boldsymbol{s}_1$, $\boldsymbol{d} = (\boldsymbol{s}_1 + \boldsymbol{s}_2)/2$, and $\mu \equiv \cos\theta = \hat{\boldsymbol{s}}\cdot\hat{\boldsymbol{d}}$ respectively.

Equation (14) with equations (15)–(17) is the key expression of our analytical model for the dipole cross-correlation function. As we will see in the next subsection, the resultant expression for the dipole moment involves only 1D integrals, and the prediction can be made much faster than that of the quasi-linear model by Saga et al. (2020), also reproducing the simulation results remarkably well. Hence, the present model can be used to systematically explore the dependence of various parameters characterizing the properties of galaxies as well as the setup of upcoming/ongoing surveys.

2.2 Cross-correlation function

We now compute the cross-correlation function and derive an analytical expression for the dipole moment. In doing so, we explicitly write the density field for the objects X as $\delta_{\rm X}^{\rm (S)}$. Then, the cross-correlation function between different species X and Y is given by

$$\xi_{\rm XY}(\boldsymbol{s}_1,\, \boldsymbol{s}_2) \equiv \left\langle \delta_{\rm X}^{\rm (S)}(\boldsymbol{s}_1)\delta_{\rm Y}^{\rm (S)}(\boldsymbol{s}_2)\right\rangle. \tag{18}$$

Taking the directional dependence of the observer's line of sight into account, the statistical homogeneity and isotropy no longer hold, and the cross-correlation function given above cannot be simply characterized as a function of the separation $s = |\boldsymbol{s}_2 - \boldsymbol{s}_1|$. Rather, it also depends on the distances to the objects X and Y, i.e. $|\boldsymbol{s}_1|$ and $|\boldsymbol{s}_2|$. Equivalently, the function $\xi_{\rm XY}$ is characterized as a function of the separation s, the mid-point distance $d = |\boldsymbol{s}_1 + \boldsymbol{s}_2|/2$, and the directional cosine between the separation vector and the mid-point vector, $\mu \equiv \hat{s}\cdot\hat{d}$, with separation vector defined by $\boldsymbol{s} \equiv \boldsymbol{s}_2 - \boldsymbol{s}_1$ (see Fig. 1 for the geometric configuration of the cross-correlation function). We shall below write the explicit dependence of $\xi_{\rm XY}$ in its argument as $\xi_{\rm XY}(s,\, d,\, \mu)$.

Substituting equation (14) into equation (18), the cross-correlation function $\xi_{\rm XY}$ is given as a collection of several pieces. Since the terms coming from the gravitational redshift effect, i.e. $\delta^{\rm (pot)}$ and $\delta^{(\epsilon_{\rm NL})}$, are supposed to be sub-dominant compared to the standard Doppler term,

we can neglect the contributions from their cross-talks. We then have

$$\begin{aligned}\xi_{\rm XY}(s,d,\mu) &\simeq \left\langle \delta_{\rm X}^{\rm (std)}(\boldsymbol{s}_1)\delta_{\rm Y}^{\rm (std)}(\boldsymbol{s}_2)\right\rangle \\ &\quad + \left\{\left\langle \delta_{\rm X}^{\rm (std)}(\boldsymbol{s}_1)\delta_{\rm Y}^{\rm (pot)}(\boldsymbol{s}_2)\right\rangle + \left\langle \delta_{\rm X}^{\rm (pot)}(\boldsymbol{s}_1)\delta_{\rm Y}^{\rm (std)}(\boldsymbol{s}_2)\right\rangle\right\} \\ &\quad + \left\{\left\langle \delta_{\rm X}^{(\epsilon_{\rm NL})}(\boldsymbol{s}_1)\delta_{\rm Y}^{\rm (std)}(\boldsymbol{s}_2)\right\rangle + \left\langle \delta_{\rm X}^{\rm (std)}(\boldsymbol{s}_1)\delta_{\rm Y}^{(\epsilon_{\rm NL})}(\boldsymbol{s}_2)\right\rangle\right\} \\ &\equiv \xi_{\rm XY}^{\rm (std)}(s,d,\mu) + \xi_{\rm XY}^{\rm (pot)}(s,d,\mu) + \xi_{\rm XY}^{(\epsilon_{\rm NL})}(s,d,\mu).\end{aligned} \tag{19}$$

Since we are particularly interested in the dipole moment of the cross-correlation function, we hereafter consider the multipole expansion of the $\xi_{\rm XY}$, taking specifically the mid-point vector, $\boldsymbol{d} = (\boldsymbol{s}_1 + \boldsymbol{s}_2)/2$, as the line-of-sight direction:

$$\xi_{{\rm XY},\ell}(s,d) = \frac{2\ell+1}{2}\int_{-1}^{1} {\rm d}\mu\ \xi_{\rm XY}(s,d,\mu)\mathcal{L}_\ell(\mu), \tag{20}$$

$$\equiv \xi_{{\rm XY},\ell}^{\rm (std)}(s,d) + \xi_{{\rm XY},\ell}^{\rm (pot)}(s,d) + \xi_{{\rm XY},\ell}^{(\epsilon_{\rm NL})}(s,d), \tag{21}$$

with $\mathcal{L}_\ell$ being the Legendre polynomials. Notice that the line-of-sight direction considered here is directional-dependent. Since we do not take the plane-parallel limit, the wide-angle effect comes to play, and the multipole moment of the correlation function, $\xi_{{\rm XY},\ell}$, is not simply given as a function of the separation, but rather given as a bi-variate function of s and d. In order to isolate the scale (i.e. separation) dependence of the multipole moment from the line-of-sight dependence, we further expand the multipole moments in powers of (s/d) as follows:

$$\xi_{{\rm XY},\ell}(s,d) = \xi_{{\rm XY},\ell}^{\rm pp}(s) + \left(\frac{s}{d}\right)\xi_{{\rm XY},\ell}^{\rm wa}(s) + \mathcal{O}\left(\left(\frac{s}{d}\right)^2\right). \tag{22}$$

The first and second terms at the right-hand side, respectively, represent the contributions from the plane-parallel limit $d \to \infty$ and the leading-order wide-angle correction. In Appendix A, substituting equations (15)–(17) into equation (19), the multipole expansion is applied up to the plane-parallel limit and wide-angle correction, and the terms defined above are derived in each contribution. The resultant expressions for the dipole moment ($\ell = 1$), including only the non-vanishing contributions, are summarized as follows (see Appendix C for other multipoles):

$$\begin{aligned}\xi_{{\rm XY},1}^{\rm (std)}(s,d) &= \left(\frac{s}{d}\right)2f(b_{\rm X}-b_{\rm Y})\left(\Xi_1^{(1)}(s) - \frac{1}{5}\Xi_2^{(0)}(s)\right) \\ &\quad + \mathcal{O}\left(\left(\frac{s}{d}\right)^2\right),\end{aligned} \tag{23}$$

$$\xi_{{\rm XY},1}^{\rm (pot)}(s,d) = -(b_{\rm X}-b_{\rm Y})\mathcal{M}\,s\,\Xi_1^{(1)}(s) + \mathcal{O}\left(\left(\frac{s}{d}\right)^2\right), \tag{24}$$

$$\begin{aligned}\xi_{{\rm XY},1}^{(\epsilon_{\rm NL})}(s,d) &= -\frac{1}{s}(\epsilon_{\rm NL,X}-\epsilon_{\rm NL,Y}) \\ &\quad \times \left(b_{\rm X}b_{\rm Y} + \frac{3}{5}(b_{\rm X}+b_{\rm Y})f + \frac{3}{7}f^2\right)\Xi_1^{(-1)}(s) \\ &\quad + \mathcal{O}\left(\left(\frac{s}{d}\right)^2\right),\end{aligned} \tag{25}$$

with the function $\Xi_\ell^{(n)}$ defined by

$$\Xi_\ell^{(n)}(s) \equiv \int \frac{k^2\,{\rm d}k}{2\pi^2}\,\frac{j_\ell(ks)}{(ks)^n}P_{\rm L}(k), \tag{26}$$

where the functions j_ℓ and $P_{\rm L}(k)$ are, respectively, the spherical Bessel function and the linear power spectrum defined in equation (A4).

The analytical expressions at equations (23)–(25) are one of the main result in this paper. As we see, the expressions of the dipole moment involve only 1D integrals, and for a given redshift z, they are characterized by the (Eulerian) bias parameters $b_{\rm X/Y}$ and the non-perturbative halo potentials $\epsilon_{\rm NL,X/Y}$, the latter of which are predicted with the NFW profile for given halo masses. We note that, in the derivations above, the magnification bias caused by the fact that the galaxy samples are flux limited is ignored (see e.g. Bonvin et al. 2014; Hall & Bonvin 2017). In Appendix D, the impact of the magnification bias, particularly induced by the Doppler effect (potentially the most dominant contribution), is discussed in detail, showing that such an effect is sub-dominant, and becomes negligibly small at higher redshifts ($z \gtrsim 0.1$).

To see the quantitative behaviour of our model presented here, in Fig. 2, the predictions of the dipole moment of the cross-correlation function, $\xi_{\rm XY,1}$, are plotted. The results at $z = 0.33$ are particularly shown, and for comparison, we also plot the measured results from the simulated halo catalogue, RayGalGroupSims,[5] which consistently take into account all the relativistic corrections by solving the geodesic equation in the presence of matter inhomogeneities. Here, the plotted results show the cross-correlation between the haloes of $\texttt{data\_H}_{1600}$ and $\texttt{data\_H}_{100}$, whose bias parameters are, respectively, given by $b_{\rm X} = 2.07$ and $b_{\rm Y} = 1.08$. In each halo sample, the potentials at the halo centre are predicted to be $\overline{\phi}_{\rm NFW,0,X} = -1.63 \times 10^{-5}$ and $\overline{\phi}_{\rm NFW,0,Y} = -0.285 \times 10^{-5}$. These values are taken from table 1 of Saga et al. (2020), assuming the NFW profile. We use them to estimate the size of the gravitational redshift effect at each halo, $\epsilon_{\rm NL,X/Y}$, and obtain $\epsilon_{\rm NL,X} > \epsilon_{\rm NL,Y} > 0$.

In Fig. 2, the black solid lines are the predictions of our analytical model. Also, their building blocks, i.e. $\xi_{\rm XY,1}^{\rm (std)}$, $\xi_{\rm XY,1}^{\rm (pot)}$, and $\xi_{\rm XY,1}^{(\epsilon_{\rm NL})}$, are separately plotted as red, blue, and magenta lines. The predicted behaviours of the dipole moment reproduce the simulation result including all the relativistic corrections well at both large and small scales. Also, it is rather close to the predictions based on the quasi-linear model of Saga et al. (2020), depicted as grey dashed lines. Thus, our present model not only successfully explain the overall trend, but also quantitatively describe the halo cross-correlation both at small and large scales. Hence, we can use it for a quantitative study on the detectability of the gravitational redshift effect. Finally, we note that the dipole moment of the cross-correlation function is dominated by the standard Doppler effect at large scales, while the gravitational redshift effect turns to be dominant at small scales, leading to the sign flip of the amplitude of $\xi_{\rm XY,1}$ at $s \approx 20$–$30\,h^{-1}$ Mpc. Thus, these behaviours play a crucial role to detect the gravitational redshift effect, and in this respect, the predictions beyond linear scales would be indispensable.

3 COVARIANCE MATRIX

In estimating the signal-to-noise ratio of the relativistic dipole in the upcoming surveys, the covariance matrix between different scales plays a crucial role. This is in particular the case for the statistics defined in the configuration space as we consider. In this paper, to compute the covariance matrix, we adopt the formalism developed by Bonvin et al. (2016), Hall & Bonvin (2017). This is a generalization of the previous formulae for the Gaussian covariance (e.g. Cohn 2006; Smith 2009; Grieb et al. 2016) to include the anisotropies in the correlation function and multitracer technique, taking also the orientation-dependent weight function into account. In Section 3.1, we present their analytical formulae for the covariance matrix. We

[5] https://cosmo.obspm.fr/public-datasets/

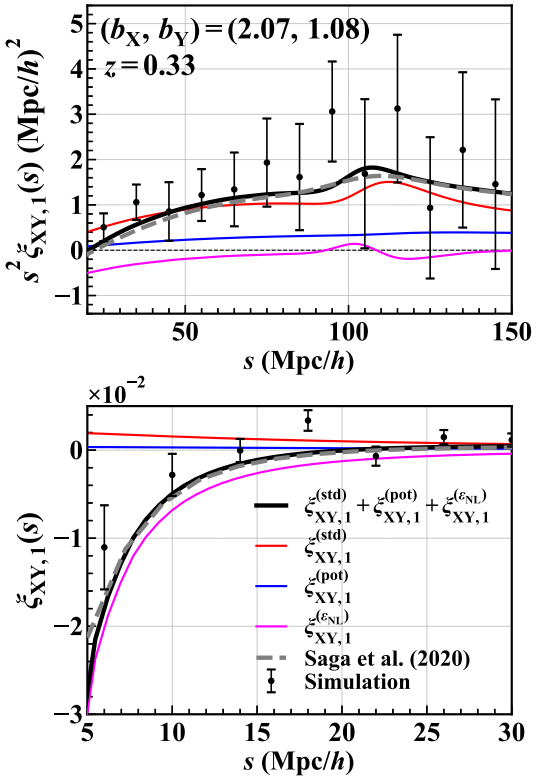

Figure 2. Dipole moment of the cross-correlation function between haloes having different bias parameters on large (top) and small (bottom) scales. The results of analytical model predictions presented in this paper are particularly shown at $z = 0.33$, together with the measured results from the halo catalogues, RayGalGroupSims, in which all possible special and general relativistic effects arising from the light propagation in an inhomogeneous universe are consistently taken into account (filled circles with errorbars). Note that in the upper panel, to clarify the large-scale behaviour, the dipole moment multiplied by the square of separation, i.e. $s^2\xi_{XY,1}$, is plotted. In each panel, black solid lines are the predictions of the analytical model (see equation (21) with equations (23)–(25)). The coloured solid lines show the breakdown of these predictions, and the red, blue, and magenta, respectively, represent the contributions from the standard Doppler ($\xi^{(std)}_{XY,1}$, equation (23)), the gravitational redshift from linear-order potential ($\xi^{(pot)}_{XY,1}$, equation (24)), and the gravitational redshift from the non-perturbative halo potential ($\xi^{(\epsilon_{NL})}_{XY,1}$, equation (25)). For reference, we also plot the predictions based on Saga et al. (2020) (grey dashed), in which the dipole cross-correlation is computed based on the Zel'dovich approximation by performing numerically seven dimensional integrals. In all predictions, we adopt the bias parameters and halo masses of the data `data_H1600` and `data_H100`, listed table 1 of Saga et al. (2020), and the potentials at the halo centre are predicted to be $\bar{\phi}_{NFW,0,X} = -1.63 \times 10^{-5}$ and $\bar{\phi}_{NFW,0,Y} = -0.285 \times 10^{-5}$ (bias parameters are also indicated in the upper panel). In the top panel, the horizontal black dotted line represents $\xi_{XY,1} = 0$.

then estimate the covariance matrix, specifically focusing on the dipole cross-correlation, in Section 3.2.

3.1 Covariance matrix of dipole cross-correlation function

To give the analytical formulae for the Gaussian covariance, let us first define the estimator for the dipole moment of the cross-correlation function. Here, we assume that the cross-correlation function can be written as a function of the separation between two objects, $\boldsymbol{s}$. This assumption is validated if we take the plane-parallel limit:

$$\hat{\xi}_{XY,1}(s) = \frac{3}{2}\int_{-1}^{1} \mathrm{d}\mu\, \mu \int \frac{\mathrm{d}^3\boldsymbol{r}}{V} \delta_X(\boldsymbol{r} - \boldsymbol{s}/2)\delta_Y(\boldsymbol{r} + \boldsymbol{s}/2), \tag{27}$$

where the quantities V and $\delta_{X/Y}$ are, respectively, the survey volume and the measured density fluctuation of the objects X/Y. The quantity μ is the directional cosine between the (fixed) line-of-sight $\hat{\boldsymbol{z}}$ and separation vectors defined by $\mu = \hat{\boldsymbol{s}} \cdot \hat{\boldsymbol{z}}$. It is to be noted that while the wide-angle effect indeed comes to play an important role in the signal part, its impact on the covariance matrix has been shown to be negligible at the scales below 190 Mpc h^{-1} (Lepori et al. 2018).

Taking the contribution arising from the discreteness of the galaxy samples into consideration, the ensemble average of the quadrature, $\delta_X(\boldsymbol{r}_1)\delta_Y(\boldsymbol{r}_2)$, becomes

$$\langle \delta_X(\boldsymbol{r}_1)\delta_Y(\boldsymbol{r}_2)\rangle = \xi_{XY}(\boldsymbol{r}_2 - \boldsymbol{r}_1) + \frac{\delta^K_{X,Y}}{n_X}\delta_D(\boldsymbol{r}_2 - \boldsymbol{r}_1), \tag{28}$$

where the quantity $\delta^K_{X,Y}$ is the Kronecker's delta and the function δ_D is the Dirac's delta function. The first term, ξ_{XY}, represents the cross-correlation function arising purely from the intrinsic clustering properties. The second term characterizes the contribution from the Poisson sampling process, which becomes non-vanishing only in the self-correlation case (i.e. X = Y and $\boldsymbol{r}_1 = \boldsymbol{r}_2$). Using the expression at equation (28), the estimator given at equation (27) is shown to be an unbiased estimator of the dipole cross-correlation, i.e. $\langle \hat{\xi}_{XY,1}(s)\rangle = \xi_{XY,1}(s)$ unless $X = Y$ and $s = 0$.

We then define the covariance of the dipole moment as follows:

$$\mathrm{COV}(s, s') \equiv \langle \hat{\xi}_{XY,1}(s)\hat{\xi}_{XY,1}(s')\rangle - \langle \hat{\xi}_{XY,1}(s)\rangle \langle \hat{\xi}_{XY,1}(s')\rangle . \tag{29}$$

With the definition given above, Hall & Bonvin (2017) derived the analytical formula for the covariance, which only involves 1D integrals:

$$\begin{aligned}\mathrm{COV}(s, s') = {} & \frac{9}{V}\int \frac{k^2\mathrm{d}k}{2\pi^2}\, j_1(ks) j_1(ks') \\ & \times \sum_{\ell_1,\ell_2} G^{\ell_2\ell_1}_{11}\left(P_{XX,\ell_1}P_{YY,\ell_2} - P_{XY,\ell_1}P_{XY,\ell_2}\right) \\ & + \frac{3}{V}\int \frac{k^2\mathrm{d}k}{2\pi^2}\, j_1(ks) j_1(ks')\left[\left(P_{XX,0} + \frac{2}{5}P_{XX,2}\right)\frac{1}{n_Y}\right. \\ & \left. + \left(P_{YY,0} + \frac{2}{5}P_{YY,2}\right)\frac{1}{n_X}\right] + \frac{\delta^K_{s,s'}}{4\pi s^2 L_p}\frac{3}{n_X n_Y V},\end{aligned} \tag{30}$$

where we define the square pixels of the side-length L_p. The coefficient $G^{\ell_2\ell_1}_{11}$ is defined by

$$G^{\ell_2\ell_1}_{\ell'\ell} = \sum_{\ell_3}(2\ell_3 + 1)\begin{pmatrix}\ell_1 & \ell_2 & \ell_3\\ 0 & 0 & 0\end{pmatrix}^2\begin{pmatrix}\ell & \ell' & \ell_3\\ 0 & 0 & 0\end{pmatrix}^2. \tag{31}$$

The functions $P_{XY,\ell}$ are the Fourier counterparts of the multipole correlation function in the plane-parallel limit:

$$\xi_{XY,\ell}(s) = (-\mathrm{i})^\ell \int \frac{k^2\,\mathrm{d}k}{2\pi^2}\, P_{XY,\ell}(k, z) j_\ell(ks). \tag{32}$$

In equation (30), the covariance matrix consists of the three contributions. The first term at the right-hand side represents the contributions arising purely from the cosmic variance, which we call the CV×CV term. On the other hand, the second term describes the cross-talk between the cosmic variance and Poisson noise, and the third term originates from the Poisson noise. We respectively call these two terms the CV×P and the P×P terms. It is to be noted

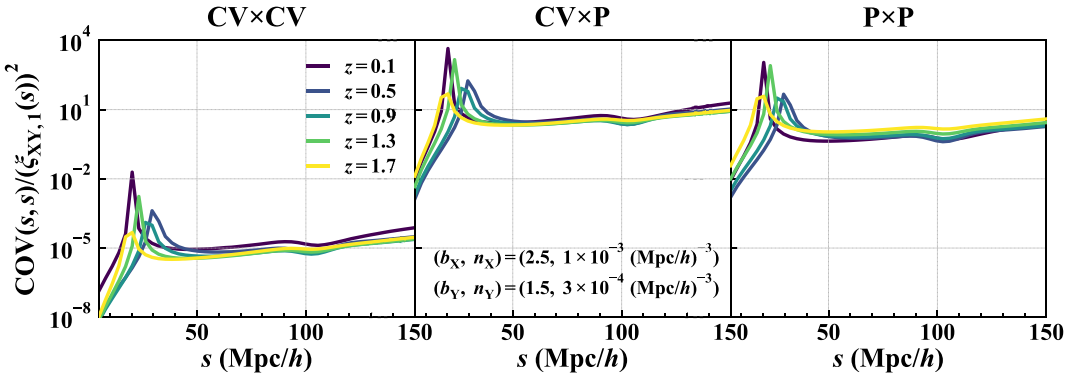

Figure 3. Diagonal components of the covariance matrix divided by the square of the dipole cross-correlation at various redshifts, plotted as a function of the separation s. From left to right, we present the contributions of the CV×CV term, the CV×P term, and the P×P term, respectively. The depth of redshift and fractional sky coverage are set to $\Delta z = 0.1$ and $f_{\rm sky} = 1$, respectively. We choose the bias parameter and number density indicated in the middle panel, which are the typical values of upcoming surveys. Note that the sharp feature near $s \approx 20$–$30\,{\rm Mpc}\,h^{-1}$ arises from the zero-crossing of the dipole moment.

that for the CV×CV term, the summation over the non-zero even multipoles ℓ_1 and ℓ_2 leads to (Bonvin et al. 2016)

$$\sum_{\ell_1,\ell_2=\mathrm{even}} G_{11}^{\ell_2\ell_1}\left(P_{\mathrm{XX},\ell_1}^{(\mathrm{std})}P_{\mathrm{YY},\ell_2}^{(\mathrm{std})}-P_{\mathrm{XY},\ell_1}^{(\mathrm{std})}P_{\mathrm{XY},\ell_2}^{(\mathrm{std})}\right)=0. \tag{33}$$

This cancellation shows that the even multipoles of the standard Doppler terms do not contribute to the CV×CV term. On the other hand, the CV×P term contains the non-vanishing even multipoles coming from the standard Doppler terms. These suggest that the CV×CV term is a sub-dominant contribution to the covariance matrix. Indeed, as we will see later, the covariance matrix is mostly dominated by the two terms, CV×P and P×P, with a negligible contribution of the CV×CV term.

To sum up, equation (30) is the covariance matrix of the dipole cross-correlation function used in the subsequent analysis. Given the multipole power spectra $P_{\mathrm{XX},\ell}$, $P_{\mathrm{YY},\ell}$ and $P_{\mathrm{XY},\ell}$, the covariance matrix $\mathrm{COV}(s, s')$ is characterized by the number densities of the objects X and Y (i.e. n_{X} and n_{Y}), the side-length of the square pixel $L_{\rm p}$, and the survey volume V. In what follows, we follow Lepori et al. (2018), and set the pixel size $L_{\rm p}$ to $2\,{\rm Mpc}\,h^{-1}$. Note that the choice of this parameter does not change the results significantly as long as we consider the scales above $L_{\rm p}$. Ignoring the survey masks and window functions, the survey volume of a hypothetical galaxy survey with the fractional sky coverage $f_{\rm sky}$ and redshift width Δz is expressed as $V = (4\pi/3)f_{\rm sky}\{r^3(z + \Delta z/2) - r^3(z - \Delta z/2)\}$, with z being the mean redshift. Here, the function $r(z)$ represents the comoving distance at redshift z. Thus, provided the survey specification parameters (i.e. $n_{\mathrm{X/Y}}$, z, Δz), the remaining pieces in estimating the covariance matrix are the multipole auto- and cross-power spectra, which are characterized in our model of cross-correlation function by the linear bias parameters $b_{\mathrm{X/Y}}$ and the non-perturbative potentials $\phi_{\mathrm{NL,X/Y}}$ for a given cosmological model. In Appendix C, we present the explicit expressions for the multipole power spectra. Since we ignored the wide-angle effect to derive the covariance matrix above, it is sufficient to consider the contributions from the plane-parallel limit, summarized in Appendix C1.

3.2 Numerical results of the dipole covariance

In this subsection, before computing the signal-to-noise ratio for upcoming surveys, we shall elucidate the basic properties of the covariance matrix. As we saw in the previous section, the covariance matrix $\mathrm{COV}(s, s')$ includes several parameters characterizing both the galaxy survey and intrinsic clustering properties. In order to relate these parameters, we adopt the halo model, and compute the covariance of the halo cross-correlation function. For haloes in the mass range $[M - \Delta M/2, M + \Delta M/2]$, the model predicts the number density n and the bias parameter b from the halo mass function, for which we use the fitting form given by Sheth & Tormen (1999). Further, through the NFW profile, the non-perturbative potential at the halo centre $\phi_{\rm NFW,0}$ is also predicted. In other words, given the halo bias and number density, the mass of haloes and the width of mass range are determined uniquely, from which one can estimate the central halo potential.[6]

With the halo model prescription mentioned above, we set the bias parameters and number densities for the halo populations X and Y to $(b_{\rm X},\ n_{\rm X}) = (2.5,\ 10^{-3}\,({\rm Mpc}\,h^{-1})^{-3})$ and $(b_{\rm Y},\ n_{\rm Y}) = (1.5,\ 3\times10^{-4}\,({\rm Mpc}\,h^{-1})^{-3})$. These are representative values among various upcoming surveys summarized in Appendix E. Then, in Fig. 3, the covariance matrix of the dipole cross-correlation function is plotted as a function of the separation, focusing specifically on the diagonal component, i.e. $s = s'$. Here, we consider a hypothetical full-sky survey ($f_{\rm sky} = 1$) having the redshift width $\Delta z = 0.1$, varying the central redshift from 0.1 (purple) to 1.7 (yellow). Dividing the diagonal covariance into the three contributions, the results normalized by the dipole moment squared, i.e. $\mathrm{COV}/(\xi_1)^2$, are separately shown: CV×CV (left-hand panel), CV×P (middle), and P×P (right-hand panel). That is, ignoring the off-diagonal components of the covariance matrix, Fig. 3 effectively represents the inverse of the square of the signal-to-noise ratio for a fixed separation. Indeed, the off-diagonal components of the covariance matrix are shown to play a minor role, and the estimated signal-to-noise mostly come from the diagonal components, as we will see later in Section 4.1.

In Fig. 3, in all three cases, the normalized covariance stays almost constant at large scales, $s \gtrsim 40\,{\rm Mpc}\ h^{-1}$, where no clear redshift dependence is seen. On the other hand, at the scales of $s = 20$–$40\,{\rm Mpc}\ h^{-1}$, we see a sharp peak. This characteristic feature merely comes from the denominator, $(\xi_1)^2$, which exhibits the zero crossing,

[6]In the actual computation, the width of the halo mass ΔM turns out to be narrow enough so that the bias parameter and halo potential averaged over the halo mass range $[M - \Delta M/2,\ M + \Delta M/2]$ are simply replaced with those evaluated at the central halo mass, M, i.e. $\langle b\rangle \simeq b(M)$ and $\langle\phi_{\rm NFW,0}\rangle \simeq \phi_{\rm NFW,0}(M)$. Also, the number density of haloes can be approximately estimated by the halo mass function ${\rm d}n/{\rm d}M$ multiplied by the width of halo mass, i.e. $n \simeq ({\rm d}n/{\rm d}M)\Delta M$.

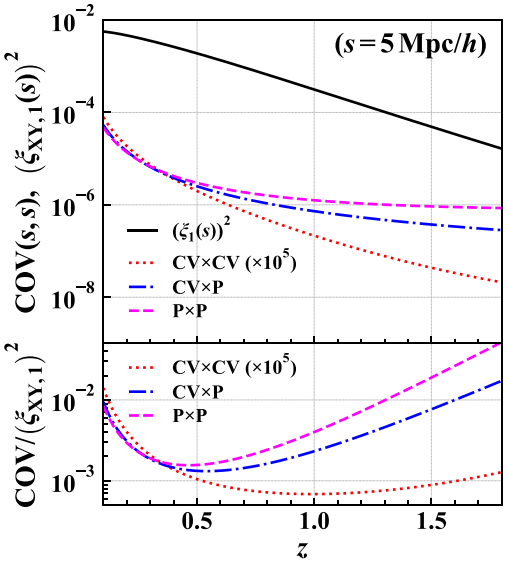

Figure 4. (Top) Redshift dependence of the diagonal components of the covariance matrix, fixing the separations to $s = s' = 5\,\mathrm{Mpc}\,h^{-1}$. Contributions from CV×CV (red dotted), CV×P (blue dot-dashed), and P×P (magenta dashed) terms are separately plotted. For comparison, the square of the dipole moment, $(\xi_1(s))^2$, is also shown (black solid). (Bottom) Redshift dependence of the ratio, $\mathrm{COV}(s, s)/(\xi_{\mathrm{XY},1}(s))^2$ at $s = 5\,\mathrm{Mpc}\,h^{-1}$, with contributions from CV×CV, CV×P, and P×P separately plotted. In both panels, the contributions from CV×CV are multiplied by 10^5 for clarity. The depth of redshift, fractional sky coverage, bias, and number density are chosen to be the same as in Fig. 3.

as shown in Fig. 2. In Saga et al. (2020), the zero-crossing point where the amplitude of the dipole moment eventually flips the sign is shown to scale as $b_{\mathrm{X}}b_{\mathrm{Y}}/(b_{\mathrm{X}} - b_{\mathrm{Y}})|\Delta\phi_{\mathrm{NL}}|\{H_0(1 + z)/H(z)\}$, with $\Delta\phi_{\mathrm{NL}}$ defined by $\Delta\phi_{\mathrm{NL}} \equiv \phi_{\mathrm{NFW,0,X}} - \phi_{\mathrm{NFW,0,Y}}$. For haloes considered here, the zero-crossing point typically appears at $s \approx 20$–$40\,\mathrm{Mpc}\,h^{-1}$ for the redshifts $0.1 \leq z \leq 1.7$. Below this scale, the normalized covariance starts to fall-off, and a rather clear redshift dependence becomes manifest, compared to the one at large scales. This implies that the signal-to-noise ratio of the dipole moment would be dominated by the behaviour below the zero-crossing point. Although these features are common in all three panels, the amplitude of the ratio for the CV×CV (left-hand panel) is substantially smaller than the other two contributions, meaning that the contribution coming from the cosmic variance is sub-dominant in the covariance matrix of the dipole moment. This is consistent with what was discussed in the previous section (see equation 33 below). The results of Fig. 3 thus show that the detectability of the relativistic dipole is mostly governed by the covariance structure of the CV×P and P×P terms below the zero-crossing point.

In Fig. 4, to see more clearly the redshift dependence of the normalized covariance at small scales, we fix the separation s to $5\,\mathrm{Mpc}\,h^{-1}$, and plot the three contributions as a function of the redshift, again focusing on the diagonal components of the covariance matrix. The upper panel of Fig. 4 shows the diagonal components of the covariance matrix and the square of the dipole moment, while the lower panel plots their ratios. It is to be noted that the ratio $\mathrm{COV}/(\xi_1)^2$ exhibit a non-monotonic behaviour. That is, the result of each contribution first decreases with the redshift, and then turns to increase at $z \gtrsim 0.5$. These behaviours come from the competition of the redshift dependence between the numerator and denominator, as is explicitly shown in the upper panel. Due to the survey volume dependence of the covariance matrix dominated by the P×P term, the numerator rapidly decreases at $z \lesssim 0.5 - 1$, but beyond that, it asymptotically approaches a constant value. On the other hand, the denominator, $(\xi_1)^2$, monotonically decreases its amplitude through the redshift evolution of the linear growth factor and the halo potential at the centre. Thus, taking the ratio, $\mathrm{COV}/(\xi_1)^2$, yields a non-trivial behaviour which takes a minimum value around $z \approx 0.5$. Although Fig. 4 shows a part of the covariance matrix, the trends seen in the diagonal component generically appear in the signal-to-noise ratio for various survey setup, and these indeed dominate the behaviours of the signal-to-noise ratio, as we will see later.

4 RESULTS: ESTIMATING SIGNAL-TO-NOISE RATIO IN UPCOMING SURVEYS

Provided the analytical model describing the relativistic dipole and the covariance matrix in the previous section, we are in a position to estimate the signal-to-noise ratio of the relativistic dipole. We define the signal-to-noise ratio, (S/N):

$$\left(\frac{\mathrm{S}}{\mathrm{N}}\right)^2 \equiv \sum_{s,s'=s_{\mathrm{min}}}^{s_{\mathrm{max}}} \xi_{\mathrm{XY},1}(s)\,\mathrm{COV}^{-1}(s, s')\,\xi_{\mathrm{XY},1}(s'), \tag{34}$$

Here, the minimum and maximum separation, s_{min} and s_{max}, have to be specified in computing the signal-to-noise ratio. In what follows, we fix the maximum separation s_{max} to $150\,\mathrm{Mpc}\,h^{-1}$. As long as we set it to a scale larger than the zero-crossing point of the dipole signal (typically at 20–40 $\mathrm{Mpc}\,h^{-1}$), the change of s_{max} hardly affects the signal-to-noise ratio. On the other hand, we see that our analytical prediction of the dipole quantitatively reproduces the simulation results even at $s \sim 5\,\mathrm{Mpc}\,h^{-1}$, below which the dipole amplitude seems to be further increased with a negative sign. However, the baryonic effects ignored in our analytical model and simulations potentially affect the dipole, and their impacts may have to be taken into account as a possible systematic effect, which needs further study. For this reason, we restrict the signal-to-noise estimation to the scales where such an effect is neglected, and set the minimum separation s_{min} to $5\,\mathrm{Mpc}\,h^{-1}$.

Then, in Section 4.1, varying the minimum separation and redshift, we study the basic behaviours of the signal-to-noise ratio, and discuss its key properties. In Section 4.2, we change parameters for galaxy surveys and galaxy/halo clustering properties to investigate the general trend of the signal-to-noise ratio. Finally, Section 4.3 estimates the signal-to-noise ratio for upcoming surveys.

4.1 Scale and redshift dependence

Let us look at the basic behaviour of the signal-to-noise ratio. First consider the dependence of the signal-to-noise ratio on the minimum separation s_{min}. In Fig. 5, assuming the same halo populations as considered in Figs 3 and 4, we plot the signal-to-noise ratio with (solid) and without (dotted) the halo potential contributions, $\xi_1^{\epsilon_{\mathrm{NL}}}$. Here, the results at different redshifts are shown as a function of s_{min}, keeping the redshift depth fixed to $\Delta z = 0.1$. Since the signal-to-noise ratio generally scales as $(\mathrm{S/N}) \propto f_{\mathrm{sky}}^{1/2}$, the plotted results are normalized by $f_{\mathrm{sky}}^{1/2}$.

Overall, the signal-to-noise ratio generally gets increased as decreasing s_{min}. A notable point is that in the presence of the halo potential term, the signal-to-noise ratio deviates from the one ignoring the halo potential at $s \lesssim 40\,\mathrm{Mpc}\,h^{-1}$. As decreasing the minimum separation, it first tends to stay constant, but eventually turns to increase, finally exceeding the signal-to-noise ratio without

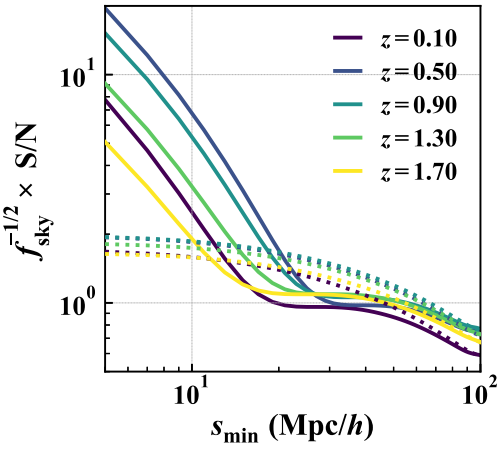

Figure 5. Signal-to-noise ratio normalized by the square root of the fractional sky coverage, $f_{\rm sky}^{-1/2}$(S/N), plotted as a function of the minimum separation $s_{\rm min}$ fixing the maximum separation to $s_{\rm max} = 150\,{\rm Mpc}\,h^{-1}$, results at various redshifts are shown in different colours. The solid and dotted lines represent the results based on our model with and without the non-perturbative correction $\xi^{(\epsilon_{\rm NL})}_{\rm XY,1}$, respectively. The redshift depth, bias, and number density are chosen to be the same as in Fig. 3.

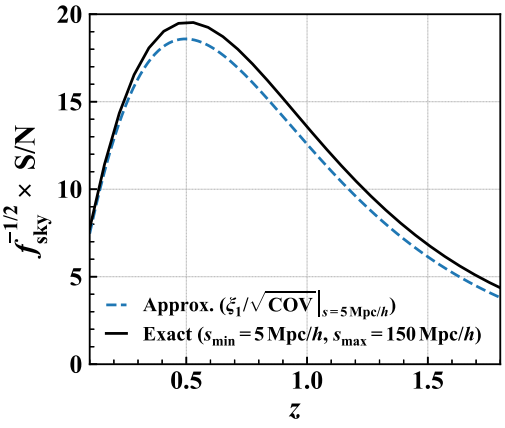

Figure 6. Redshift dependence of the signal-to-noise ratio normalized by the fractional sky coverage, $f_{\rm sky}^{-1/2}$(S/N), fixing the minimum and maximum separations to $s_{\rm min} = 5\,{\rm Mpc}\,h^{-1}$ and $s_{\rm max} = 150\,{\rm Mpc}\,h^{-1}$, respectively (black solid). The redshift depth, bias, and number density are chosen to be the same as in Fig. 3. The blue-dashed line represents the ratio, $\xi_{\rm XY,1}(s)/\sqrt{\rm COV}(s,\,s)$, at $s = 5\,{\rm Mpc}\,h^{-1}$, which approximately describes the black-solid line.

the halo potential contribution. These behaviours are indeed expected from the behaviour of the signal part, $\xi_{\rm XY,\,1}$. That is, the plateau and amplification of the signal-to-noise ratio are, respectively, linked to the sign flip and the sharp drop with negative amplitude of the dipole cross-correlation function, as shown in Fig. 2. Thus, the signal-to-noise ratio at the small minimum separation can be dominated by the gravitational redshift effect from the halo potential, and because of this, the dipole signal would be detectable at a statistically significant level.

In Fig. 5, another notable point is that the signal-to-noise ratio in the presence of halo potential contribution shows a non-trivial redshift dependence on its amplitude at $s_{\rm min} \lesssim 10\,{\rm Mpc}\,h^{-1}$. To look closely at the redshift dependence, we next plot in Fig. 6 the signal-to-noise ratio as a function of the redshift, fixing the minimum separation to $s_{\rm min} = 5\,{\rm Mpc}\,h^{-1}$. The result depicted as a black solid line has a peak at $z \approx 0.5$. Ignoring the contribution of the off-diagonal covariance, this non-monotonic behaviour is indeed inferred from the lower panel of Fig. 4, where we see the diagonal covariance normalized by $(\xi_1)^2$ has a minimum at $z \approx 0.5$. This indicates that the estimated signal-to-noise ratio is dominated by the contribution from the diagonal part of the covariance matrix, which is mainly determined by the terms CV×P and P×P. To prove this, in Fig. 6, we plot the ratio, $\xi_{\rm XY,1}(s)/{\rm COV}(s,\,s)$, evaluated at $s = 5\,{\rm Mpc}\,h^{-1}$ (blue dashed). We then find that the resultant ratio nicely explains the redshift dependence of the signal-to-noise ratio. Thus, the non-monotonic redshift dependence of the signal-to-noise ratio, having a maximum at $z \approx 0.5$, is shown to be originated from the two competitive behaviours of the cross-correlation function and diagonal covariance, as shown in Fig. 4. We will see below that based on the halo model prescription, these are rather generic features, irrespective of the survey parameters.

4.2 Dependence of target samples

So far, we have studied the behaviours of the covariance matrix and signal-to-noise ratio for specific halo samples, fixing the halo bias and halo number density, $(b_{\rm X/Y},\,n_{\rm X/Y})$. Here, we investigate the dependence of the halo samples on the signal-to-noise ratio. To do this, we vary the parameters $b_{\rm X}$, $n_{\rm X}$, and $n_{\rm Y}$. To be precise, we first set the bias for the halo sample Y to $b_{\rm Y} = 1$ (or 1.5). We then compute the signal-to-noise ratio for various set of parameters $b_{\rm X}$, $n_{\rm X}$, and $n_{\rm Y}$, with $b_{\rm X}$ being larger than $b_{\rm Y}$. Note that we ignore the contributions from the magnification bias, among which the most dominant contribution coming from the Doppler effect is discussed in Appendix D, showing it to be negligible. The results normalized by $f_{\rm sky}^{1/2}$ are plotted as a function of the halo bias $b_{\rm X}$ and the central redshift of the surveys, shown in Figs 7 and 8. Here, the redshift depth of the survey is fixed to $\Delta z = 0.1$. Note that given the halo bias and number density, one can uniquely determine the halo mass range, from which the halo potential is predicted through the NFW profile, as we did in Section 3.2.

In Figs 7 and 8, the estimated results of $f_{\rm sky}^{-1/2}$(S/N) are shown for the haloes with the number density of $n_{\rm X/Y} = 3 \times 10^{-5}$, 10^{-4}, 3×10^{-4}, and 10^{-3}, restricting the cases to $n_{\rm X} \leq n_{\rm Y}$. In all cases, we see that the signal-to-noise ratio has a peak at $z \approx 0.5$. In particular, for the halo samples having the large number density $n_{\rm X} = n_{\rm Y} = 10^{-3}\,{\rm Mpc}\,h^{-1}$ (bottom right-hand panel), the signal-to-noise ratio reaches $f_{\rm sky}^{-1/2}\,({\rm S/N}) = 45.8$ and 75.5, respectively in Figs 7 and 8, which correspond to the halo samples with the biases of $(b_{\rm X},\,b_{\rm Y}) = (3,\,1)$ and $(b_{\rm X},\,b_{\rm Y}) = (3.5,\,1.5)$. Comparing between the results in both figures, while the width of the plot range in the vertical axis are the same, i.e. $\Delta b = b_{\rm X} - b_{\rm Y} = 2$, the resultant signal-to-noise ratios are overall enhanced in the cases with $b_{\rm Y} = 1.5$ (Fig. 8). Ignoring the halo potential contribution, the dipole moment of the cross-correlation function scales as $\xi_{\rm XY,1} \propto (b_{\rm X} - b_{\rm Y})$ (see equations 24 and 23). That is, in the absence of the halo potential, the resultant signal-to-noise ratio should be the same in both Figs 7 and 8. This implies that the difference between the two figures is attributed to the contribution from the halo potential in the dipole moment. Since the haloes with a larger bias tend to have larger halo masses, the halo potential also becomes deeper as increasing the bias. The important point is that the depth of the potential is not linearly proportional to the halo mass. As a result, the difference of the potential $\Delta\phi_{\rm NL} = \phi_{\rm NFW,0,X} - \phi_{\rm NFW,0,Y}$ gets large as increasing the bias or halo mass, leading to an additional enhancement of the signal-to-noise ratio for haloes with large biases.

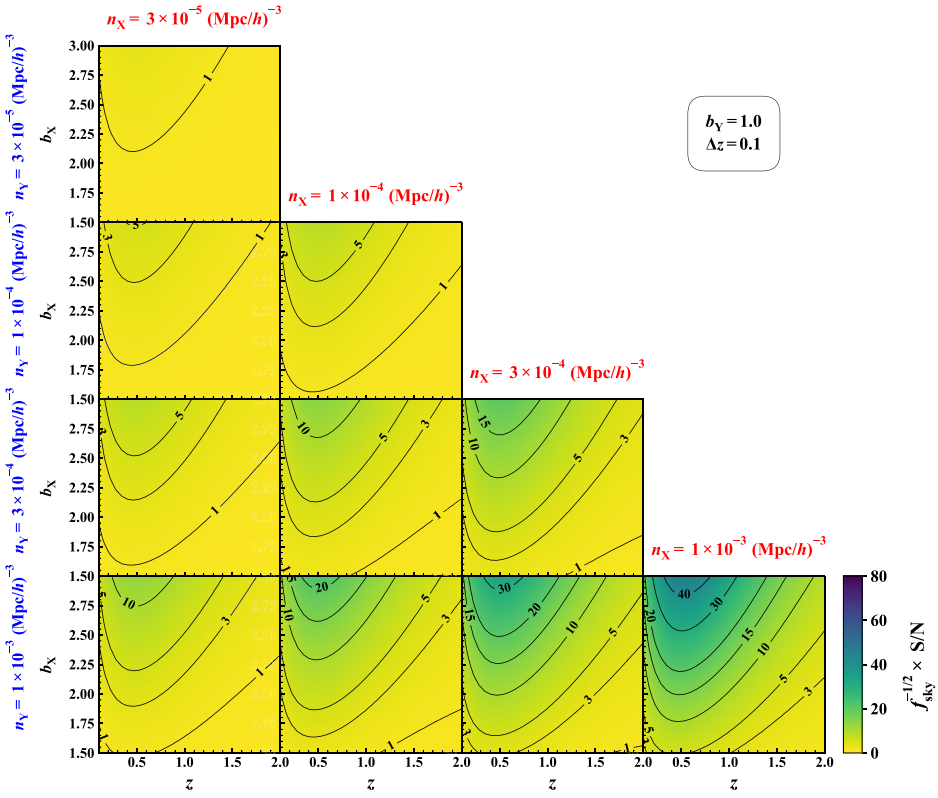

Figure 7. 2D plot of the signal-to-noise ratio as a function of b_X and z, where b_X is the bias of massive halo populations and z is the redshift of the survey assuming the range $[z - 0.05, z + 0.05]$. The bias of less massive halo population is fixed to $b_Y = 1.0$. In each panel, the colour scale and black contours indicate the signal-to-noise ratio normalized by the square of the fractional sky coverage, $f_{sky}^{-1/2}$(S/N) (see the rightmost colour bar). Panels show the results adopting various number densities of halo populations, n_X and n_Y, ranging from 3×10^{-5} (Mpc h^{-1})$^{-3}$ to 10^{-3} (Mpc h^{-1})$^{-3}$, as indicated in the blue and red texts.

The behaviours shown in Figs 7 and 8 provide a useful guideline to discuss the feasibility to detect the relativistic dipole. In the next subsection, based on these results, we will estimate the detectability of the dipole moment.

4.3 Future observations

Having studied the general behaviours of the signal-to-noise ratio, let us now focus on the upcoming galaxy surveys, and estimate the signal-to-noise ratio of the dipole moment. The surveys considered here are listed in Table 1. In Fig. 9, we summarize the redshift dependence of the bias and number density for the target galaxies in each survey, which are based on Tables E1–E6, summarized in Appendix E.

In detecting the relativistic dipole, we need two galaxy samples having different values of the bias parameters. There are in general two strategies to measure the dipole cross-correlation functions. One is to divide a single galaxy population in a given survey into two subsamples. Another is to cross-correlate two different samples obtained from multiple surveys (or single survey). In what follows, we set $s_{min} = 5\,\mathrm{Mpc}\ h^{-1}$ and $s_{max} = 150\,\mathrm{Mpc}\ h^{-1}$, and separately consider the two cases in estimating the signal-to-noise ratios.

4.3.1 Cross-correlating two divided populations from the single target

We first focus on a single galaxy population, and dividing the sample into two subsamples, we take a cross-correlation between them. Depending on how we divide the sample into two, the number densities and the bias parameters of the two subsamples differ from each other as well as those of the original sample. Thus, the signal-to-noise ratio of the relativistic dipole varies on how we divide the sample into two. Here, we shall estimate the best signal-to-noise ratio based on the halo model prescription, assuming that the galaxies of our interest follow the halo distribution whose halo masses are larger than M_{min}. We then divide the galaxies into two subsamples Y and X hosted, respectively, by the haloes with the mass ranges $[M_{min}, M_*]$ and $[M_*, \infty]$.

Denoting the number density of the galaxies before division by n_{obs}, their bias parameters $b_{X/Y}$ and number densities $n_{X/Y}$ are given by

$$n_X(M_*) = n_{obs}\frac{\int_{\ln M_*}^{\infty}\frac{dn}{d\ln M}\,d\ln M}{\int_{\ln M_{min}}^{\infty}\frac{dn}{d\ln M}\,d\ln M}, \tag{35}$$

$$b_X(M_*) = \frac{\int_{\ln M_*}^{\infty} b_{ST}(M)\frac{dn}{d\ln M}\,d\ln M}{\int_{\ln M_*}^{\infty}\frac{dn}{d\ln M}\,d\ln M}, \tag{36}$$

for the massive population, and

$$n_Y(M_*) = n_{obs}\frac{\int_{\ln M_{min}}^{\ln M_*}\frac{dn}{d\ln M}\,d\ln M}{\int_{\ln M_{min}}^{\infty}\frac{dn}{d\ln M}\,d\ln M}, \tag{37}$$

$$b_Y(M_*) = \frac{\int_{\ln M_{min}}^{\ln M_*} b_{ST}(M)\frac{dn}{d\ln M}\,d\ln M}{\int_{\ln M_{min}}^{\ln M_*}\frac{dn}{d\ln M}\,d\ln M}. \tag{38}$$

for the less massive population. Here, the functions b_{ST} and $dn/d\ln M$ are the halo bias and mass function, for which we use the expressions given by Sheth & Tormen (1999). Note that we also examined the

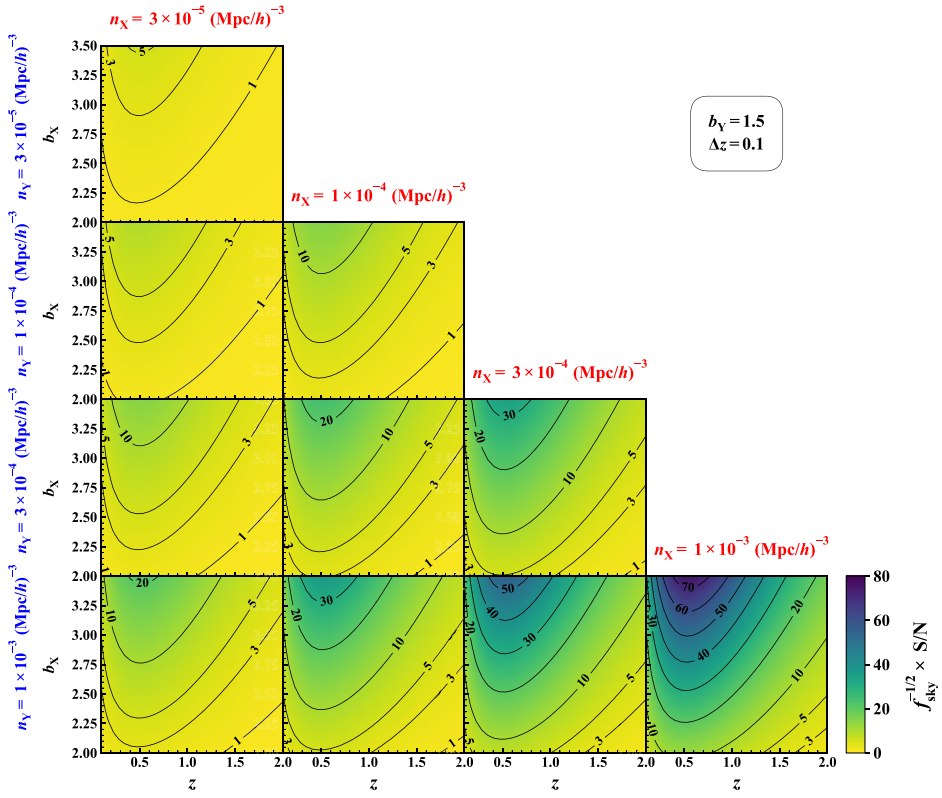

Figure 8. Same as Fig. 7 but for the bias of less massive halo population, $b_Y = 1.5$.

Table 1. The upcoming surveys considered in this paper. In Appendix E, we summarize each survey parameters in Tables E1–E6.

Survey	Target samples	f_{sky} (deg^2)	Redshift range
DESI	BGS	14 000	[0.05, 0.45]
	LRG	14 000	[0.65, 1.15]
	ELG	14 000	[0.65, 1.65]
Euclid	Hα emitter	15 000	[0.9, 1.8]
PFS	(O II) ELG	1464	[0.6, 2.4]
SKA1	H I galaxies	1500	[0.05, 0.45]
SKA2	H I galaxies	30 000	[0.23, 1.81]

prescription given by Tinker et al. (2008, 2010), and found that the estimated halo potential changes at most by a few per cent, and thus the results are insensitive to the choice of the model. With this prescription, we have $b_X > b_Y$, and $n_{obs} = n_X(M_*) + n_Y(M_*)$. Note that, because of the idealistic treatment in the above, i.e. two subsamples having the mass ranges $[M_{min}, M_*]$ and $[M_*, \infty]$, the value of the parameter M_* tends to be large when we obtain the best signal-to-noise ratio. In Appendix E, we summarize the ratio of the number densities $n_X(M_*)/n_{obs}$ when the signal-to-noise ratio reaches its maximum. This will give us a guideline for future observations when we divide the sample into two subsamples.

In the expressions given above, the minimum halo mass M_{min} and the threshold mass M_* are the parameters, but the former is determined by the bias of the original sample, b_{obs}:

$$b_{obs} = \frac{\int_{\ln M_{min}}^{\infty} b_{ST}(M) \frac{dn}{d\ln M} d\ln M}{\int_{\ln M_{min}}^{\infty} \frac{dn}{d\ln M} d\ln M}. \quad (39)$$

That is, provided the value of b_{obs} for a given survey, the minimum mass M_{min} is obtained by solving equation (39). Thus, the threshold mass is the only free parameter that controls the signal-to-noise ratio, and we determine it by maximizing the signal-to-noise ratio. Note that in evaluating (S/N), the halo potential contribution to the relativistic dipole, $\phi_{NFW,0,X}$ and $\phi_{NFW,0,Y}$, are averaged over the mass ranges $[M_*, \infty]$ and $[M_{min}, M_*]$, respectively, as similarly to the biases given in equations (36) and (38). We note that, in the lowest redshift bin of SKA1 ($z = 0.05$), the bias parameter given in Bull et al. (2015) does not fulfill the condition given at equation (39), and we cannot obtain the solution for M_{min}. Hence, only for this case, we do not use equation (39), but instead fix the minimum mass to $M_{min} = 10^8\, M_\odot\, h^{-1}$, based on Yahya et al. (2015).

Top panel of Fig. 10 shows the results of the optimal signal-to-noise ratio for each galaxy population of upcoming surveys. We find that among those considered, the DESI-BGS sample gives the largest S/N. Since the cosmic variance is not the main source for the statistical error, surveys with a larger number density can give a higher signal-to-noise ratio, irrespective of the survey volume. Further increasing the difference of the biases b_X–b_Y, the signal-to-noise ratio for the DESI-BGS sample eventually reaches the maximum value S/N = 23 at $0.1 \leq z \leq 0.2$, above which the signal-to-noise ratio sharply falls off due to a rapid decrease of the number density. Note cautiously that with the minimum mass M_{min} determined by the bias b_{obs}, the number density of the DESI-BGS sample n_{obs} exceeds the one inferred from the halo mass function. This implies that the host halo generally contains multiple DESI-BGS samples. Since these galaxies do not necessarily reside at the halo centre, the non-perturbative potential contribution to the relativistic dipole would be suppressed. In this respect, the resultant S/N for the DESI-BGS samples should be considered as a theoretical upper

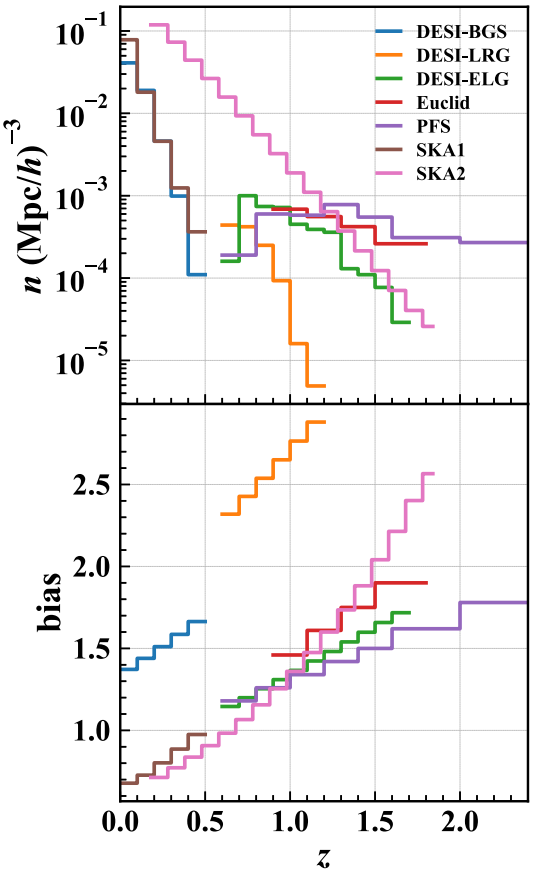

Figure 9. Expected number density of galaxies (top) and bias parameter (bottom) for the surveys listed in Table 1. The plotted data are taken from the tables summarized in Appendix E.

bound. A more realistic estimation of the signal-to-noise ratio needs a model based on the halo occupation distribution approach. We leave specific modelling for the DESI-BGS samples to our future work. This issue is a priori less severe in other surveys where the halo occupation number is less than unity.

Apart from the low-z galaxy survey, other notable results having large signal-to-noise ratios ($1 \lesssim$ S/N) are found from the *Euclid*, DESI-ELG, SKA2, and DESI-LRG samples, among which the last two exceed S/N = 10 around $z \approx 0.7$. Interestingly, looking at Fig. 9, the number density of the DESI-LRG sample is substantially smaller than that of the SKA2 by more than one order of magnitude. However, the bias of DESI-LRG sample is larger than that of the SKA2 sample, and the difference amounts to $\Delta b \approx 1.5$. As a result, at $z \approx 0.7$–0.8, their signal-to-noise ratios are comparable and reach maximum values. This implies that for a solid detection of the relativistic dipole, samples having a large bias are preferable. In other words, samples with a small bias $b \approx 1$–1.5 tend to have small signal-to-noise ratios, as indeed shown for other surveys in Fig. 10. It is to be noted that even though the bias and number density of the samples considered are not constant over the redshifts, the overall trends seen in Fig. 10 resemble those shown in Figs 7 and 8.

Finally, to illustrate how the S/N shown in the left-hand panel of Fig. 10 is robust and optimal against the strategies to create two subsamples, we consider alternative ways to divide the sample into two, and estimate their signal-to-noise ratios. The bottom panel of Fig. 10 plots the results derived from the two strategies. One is to

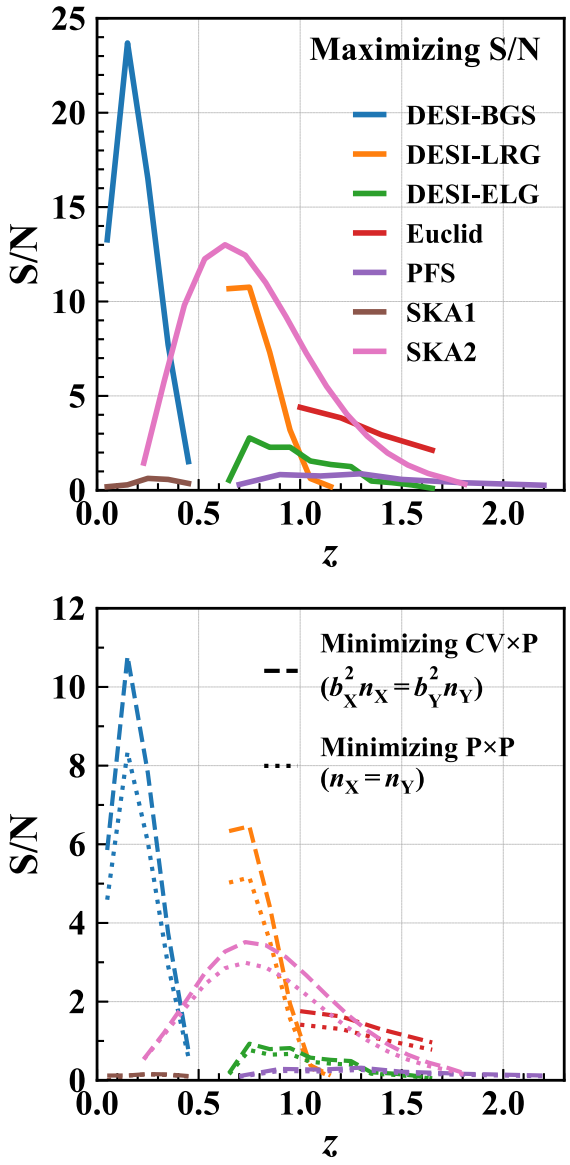

Figure 10. Expected signal-to-noise ratio for the surveys listed in Table 1, using the single galaxy population. (Top) Dividing the sample into two subsamples to cross-correlate, we choose the threshold halo mass M_* so that the signal-to-noise ratio is maximized at each redshift bin (see the text in detail in Section 4.3.1). (Bottom) Same as the top panel, but the threshold halo mass M_* is chosen so that the CV×P (dashed lines) and P×P (dotted lines) contributions are minimized by imposing the conditions, $b_X^2 n_X = b_Y^2 n_Y$ and $n_X = n_Y$, respectively. Note that accounting for the halo occupation number, the signal-to-noise ratio for DESI-BGS would be optimistic (see the main text, fourth paragraph in Section 4.3.1 for details).

minimize the CV×P term in the covariance matrix (dashed), and the other is to minimize the P×P term (dotted). Recalling from equation (30) that the CV×P and P×P terms are roughly proportional to $\mathrm{COV}_{XY} \propto b_X^2/n_Y + b_Y^2/n_X$ and $1/(n_X n_Y)$, the conditions that minimize these two contributions are found to be $b_X^2 n_X = b_Y^2 n_Y$ and $n_X = n_Y$ (a popular choice), respectively. In our treatment, these conditions are satisfied by choosing an appropriate mass threshold M_*. Note that these strategies are considered from a perspective of the error minimization, ignoring the role of the signal part itself. In this respect, they do not necessarily provide an optimal signal-to-

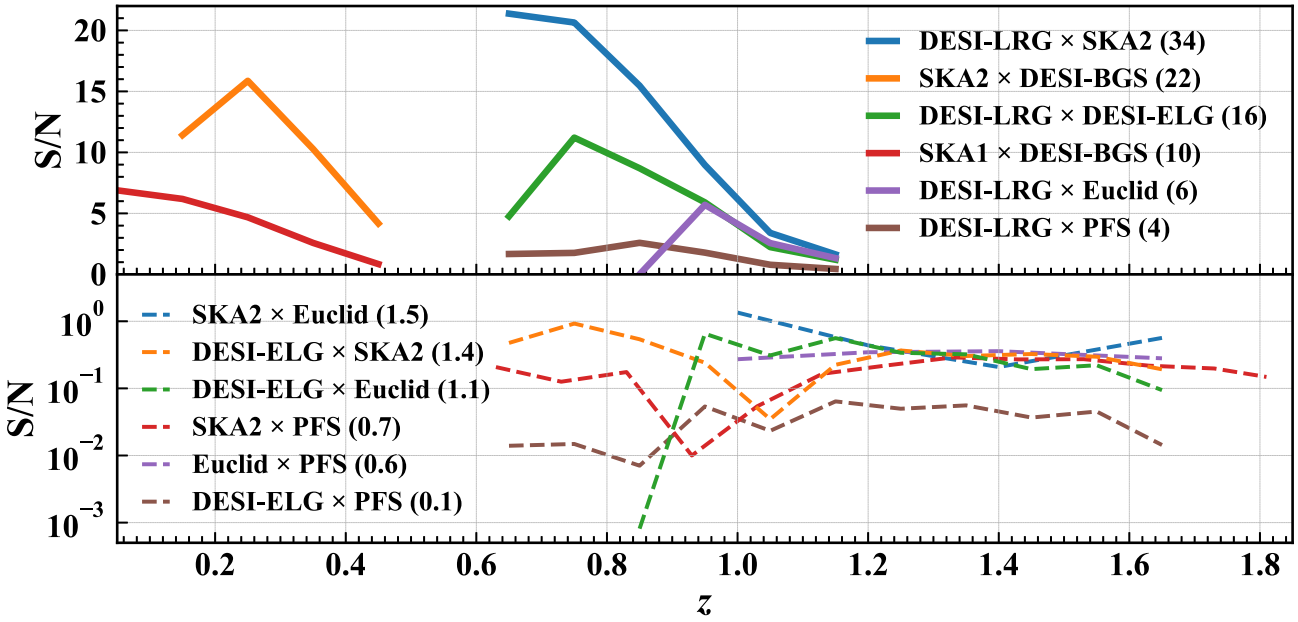

Figure 11. Expected signal-to-noise ratio for the cross-correlation between two different samples without creating subsamples. The target samples are obtained either from different surveys or single survey listed in Table 1. The top (bottom) panel summarizes the results for which the cumulative signal-to-noise ratio combining multiple redshift slices, given by $\sqrt{\sum_z (\mathrm{S/N})^2}$, is greater (less) than 2. The estimated values of the cumulative signal-to-noise ratio are summarized in the legend (see parentheses). Note that the signal-to-noise ratio may be optimistic for the cases including the DESI-BGS sample (see the fourth paragraph in Section 4.3.1 for details).

noise ratio. Accordingly, the signal-to-noise ratio is changed, and one finds that in all surveys considered, the resultant value of S/N almost halves the optimal signal-to-noise ratio. The results imply that both the CV×P and P×P contributions play an equal role in estimating the signal-to-noise ratio, suggesting that a careful sample cut needs to be considered in practical observations in optimizing the S/N.

4.3.2 *Cross-correlating two different targets*

The signal-to-noise ratio of the relativistic dipole considered in Section 4.3.1 depends on how we divide the sample into two subsamples, and thus it would be sensitive to the internal properties of the galaxy populations. Now, let us next consider the cross-correlation between two different samples, obtained either from different surveys or single survey, without creating subsamples. This is achieved with the samples whose observed regions are overlapped with each other. In order to maximize the detectability of the relativistic dipole, we here consider an idealistic setup where the observed areas of galaxy surveys considered are perfectly overlapped with each other without survey masks. To be precise, based on Tables E1–E4 in Appendix E, we follow the halo model prescription in Section 4.3.1 and first determine the minimum halo mass $M_{\rm min}$ in each sample from equation (39). Then, we estimate the non-perturbative contribution to the halo potential, $\phi_{\rm NFW,0}$, which we take an average over the mass range $[M_{\rm min}, \infty]$. Plugging this potential into the dipole cross-correlation function, the signal-to-noise ratio is computed, and we examine all possible combinations of overlapping surveys in redshift. In practice, one may encounter the case that redshift slices of the two samples do not coincide with each other. In such a case, we adopt the redshift bin for the sample having a larger value of the bias as our fiducial redshift slice, and compute the signal-to-noise ratio for this redshift bin, with the bias and number density of the less biased galaxies redefined, as described in Appendix E2. This treatment would lead to an optimistic S/N, particularly for the cases including the DESI-BGS sample.

Fig. 11 summarizes the results of the signal-to-noise ratio for various cross-correlated galaxy samples. The top (bottom) panels show the results in which the cumulative signal-to-noise ratio combining all redshift bins, $\sqrt{\sum_z (\mathrm{S/N})^2}$, is larger (smaller) than 2, for presentation purpose. We find that the cross-correlation between DESI and SKA2 surveys gives a large value of S/N, and a statistically significant detection of the relativistic dipole is expected particularly for DESI-BGS and SKA2 (purple), DESI-LRG and SKA2 (blue). Also, the cross-correlation between the DESI samples, i.e. LRG and ELG (orange), gives a large signal-to-noise ratio S/N ≈ 10 around $z = 0.7$. The detection of the dipole signal from these surveys would provide a new way to probe gravity at cosmological scales. Furthermore, making use of the cross-correlation technique, the signal-to-noise ratio becomes improved, and SKA1 and *Euclid* surveys are capable of detecting the relativistic dipole at high statistical significance (S/N $\gtrsim 5$) if we combine them with the DESI-LRG and *Euclid* galaxy samples, respectively. The results having a small signal-to-noise ratio, shown in the bottom panel, mainly come from the cross-correlation between emission-line galaxies which typically have small bias parameters. Compared to the single-tracer cases in Section 4.3.1, the advantage of the present method is that the impact of the shot noise contribution is mitigated, also helping us to reduce unknown systematics inherent in each survey. In this respect, combining multiple tracers would be rather suited for detecting the dipole moment induced by the gravitational redshift effects.

5 SYSTEMATIC EFFECTS FROM OFF-CENTRED GALAXIES

So far, we have considered the detectability of the relativistic dipole, taking only the gravitational redshift and Doppler effects

into account. In this section, we discuss a potential impact of the systematics ignored so far.

In our analytical treatment, one crucial assumption is that each of the galaxies to cross-correlate strictly reside at the halo centre, and thus no virialized random motion is invoked. This is an idealistic situation, and there are galaxies whose positions are away from the halo centre (e.g. Hikage et al. 2013). The off-centred galaxy positions lead to two possible systematics in the dipole signal. One is the diminution of the non-perturbative halo potential contribution to the gravitational redshift effect. Another is to introduce the virialized random motion to the off-centred galaxies. This can give a non-negligible amount of the transverse Doppler effect as the second-order special relativistic effect, which is known to produce the dipole cross-correlation signal (Kaiser 2013; Zhao, Peacock & Li 2013; Cai et al. 2017; Zhu et al. 2017; Breton et al. 2019). Note that there are other relativistic effects that induce the dipole asymmetry in the cross-correlation function, and their impacts on the detection of gravitational redshift effect have been studied in both numerical and analytical treatments (Zhu et al. 2017; Breton et al. 2019; Di Dio & Seljak 2019; Beutler & Di Dio 2020). Below, we analytically estimate the impacts of these two effects on the dipole signal.

Let us first discuss the suppressed gravitational potential. Following Hikage et al. (2013), we introduce the probability distribution function of the galaxy position inside each halo, $p_{\rm off}$, normalized as follows:

$$\int_0^{r_{\rm vir}} 4\pi r^2 p_{\rm off}(r; R_{\rm off})\,{\rm d}r = 1. \tag{40}$$

We model it to be Gaussian distribution, i.e. $p_{\rm off}(r; R_{\rm off}) \propto \exp(-(r/R_{\rm off})^2/2)$ with $R_{\rm off}$ being the offset parameter. Using the distribution function $p_{\rm off}$, the halo potential at the off-centred galaxy position can be estimated to be

$$\overline{\phi}_{\rm NFW}(z, M, R_{\rm off}) = \int_0^{r_{\rm vir}} 4\pi r^2 \phi_{\rm NFW}(r, z, M) p_{\rm off}(r; R_{\rm off})\,{\rm d}r, \tag{41}$$

where the explicit form of the NFW potential $\phi_{\rm NFW}(r, z, M)$ can be found in Appendix D of Saga et al. (2020). Note that in the limit of $R_{\rm off} \to 0$, the distribution function becomes $p_{\rm off}(r) = \delta_{\rm D}(r)/(4\pi r^2)$, and we consistently reproduce $\overline{\phi}_{\rm NFW}(z, M, R_{\rm off}) = \phi_{\rm NFW,0}(z, M)$. Adopting equation (41), we substitute $\overline{\phi}_{\rm NFW}$ into the expression of $\epsilon_{\rm NL}$ in equation (13), instead of the central potential $\phi_{\rm NFW,0}$. Then the dipole cross-correlation with the suppressed halo potential contribution is estimated through the analytical formulas in Section 2.2.

Next consider the transverse Doppler effect from the off-centred galaxies. To estimate its qualitative impact, we compute the velocity dispersion of galaxies, σ_v^2, which is expressed as a sum of the two contributions (e.g. Sheth & Diaferio 2001):

$$\sigma_v^2(r, z, M) = \sigma_{\rm vir}^2(r, z, M) + \sigma_{\rm halo}^2(z, M). \tag{42}$$

Here, the first and second terms at the right-hand side are originated, respectively, from the virial motion within a halo and the large-scale coherent motion of the host haloes. Note that the second term is non-vanishing even if the galaxies reside at the centre of the haloes. Although we include it for self-consistency, we confirmed that the transverse Doppler effect is dominated by the virial motion.

To compute the velocity dispersion of the virial motion, $\sigma_{\rm vir}^2$, we adopt the halo model prescription and use the analytical formula for the velocity dispersion of the NFW density profile (see equation 14 of Łokas & Mamon 2001):

$$\sigma_{\rm vir}^2(r, z, M) = \alpha(r, z, M)\frac{GM}{r_{\rm vir}}, \tag{43}$$

with the function $\alpha(r, z, M)$ given by

$$\alpha(r, z, M) = \frac{3}{2}c^2 g(c) x (1+cx)^2 \left[6{\rm Li}(-cx) + \pi^2 - \ln(cx) - \frac{1}{cx} - \frac{1}{(1+cx)^2} - \frac{6}{1+cx} + 3\ln^2(1+cx) + \ln(1+cx)\left(1 + \frac{1}{(cx)^2} - \frac{4}{cx} - \frac{2}{1+cx}\right)\right], \tag{44}$$

where the quantities c, x, and function ${\rm Li}(x)$, respectively, stand for the concentration parameter (Bullock et al. 2001; Cooray & Sheth 2002), the radius normalized by the virial radius, $x \equiv r/r_{\rm vir}$, and the logarithmic integral function. The function $g(c)$ is defined as $g(c) \equiv [\ln(1+c) - c/(1+c)]^{-1}$.

For the velocity dispersion, $\sigma_{\rm halo}^2$, we estimate it using the prediction of the peak theory based on the linear Gaussian density fields (Bardeen et al. 1986; Sheth & Diaferio 2001):

$$\sigma_{\rm halo}^2(z, M) = (aHfD_+)^2 \sigma_{-1}^2(M)\left(1 - \frac{\sigma_0^4(M)}{\sigma_1^2(M)\sigma_{-1}^2(M)}\right), \tag{45}$$

where we define the function σ_n by

$$\sigma_n^2(M) = \int \frac{k^2 {\rm d}k}{2\pi^2} k^{2n} P_{\rm L}(k) W^2(kR). \tag{46}$$

Here the function $W(x) = 3j_1(x)/x$ is the Fourier transform of the real space top-hat window function, and the radius R is related to the mass of the halo M through $M = 4\pi\bar{\rho}R^3/3$, where the quantity $\bar{\rho}$ is the background matter density.

Given the velocity dispersion from the above analytical formulae, the total impact of the off-centring effects, including the transverse Doppler effect, is estimated by replacing the $\epsilon_{\rm NL}$ in equation (13) with

$$\epsilon_{\rm NL} \to \overline{\epsilon}_{\rm NL} = -\frac{1}{aH}\overline{\phi}_{\rm NFW}(z, M, R_{\rm off}) + \frac{1}{aH}\frac{1}{2}\overline{\sigma}_v^2(z, M, R_{\rm off}). \tag{47}$$

Here, the second term at the right-hand side represents the transverse Doppler effect, and the velocity dispersion, $\overline{\sigma}_v^2$, is obtained by averaging σ_v^2 over the radius with the probability distribution function, $p_{\rm off}$, similarly to the first term (see equation 41). Equation (47) provides an analytical way to estimate the impact of the off-centring effects on the dipole signal, but we note that there are several assumptions and simplifications in deriving equation (47). For instance, the velocity dispersion $\sigma_{\rm vir}^2$ at equation (44) has been derived under the assumption of the isotropic velocity distribution, which is known to be inaccurate for the haloes in N-body simulations. Further, the bulk velocity dispersion $\sigma_{\rm halo}^2$ at equation (45) is based on the linear theory, and it underpredicts the actual velocity dispersion for simulated haloes. Our primary focus here is to study the qualitative impacts of the off-centring effects, and a more accurate estimation will have to be addressed based on numerical simulations. This is left for our future work.

Fig. 12 shows the impacts of the off-centring effects on the dipole moment obtained from the analytical treatment at redshifts, $z = 0.1$ (top), 0.9 (middle), and 1.7 (bottom). Here, we particularly focus on the dipole cross-correlation function at $s = 5$–$20\,{\rm Mpc}\,h^{-1}$, where the gravitational redshift effect dominates the standard Doppler effect, and it dominantly contributes to the signal-to-noise ratio. To elucidate how their impacts are changed with the off-centring parameter, we examine the two cases: $R_{\rm off} = 0.1\,r_{\rm vir}$ (left-hand panel) and $0.2\,r_{\rm vir}$ (right-hand panel), as typical values considered in Hikage et al. (2013). In each panel, black solid and dashed lines are the dipole cross-correlation functions with and without the systematics, respectively (labelled by $\xi_1(\overline{\epsilon}_{\rm NL})$ and $\xi_1(\epsilon_{\rm NL})$ in Fig. 12). Overall, the

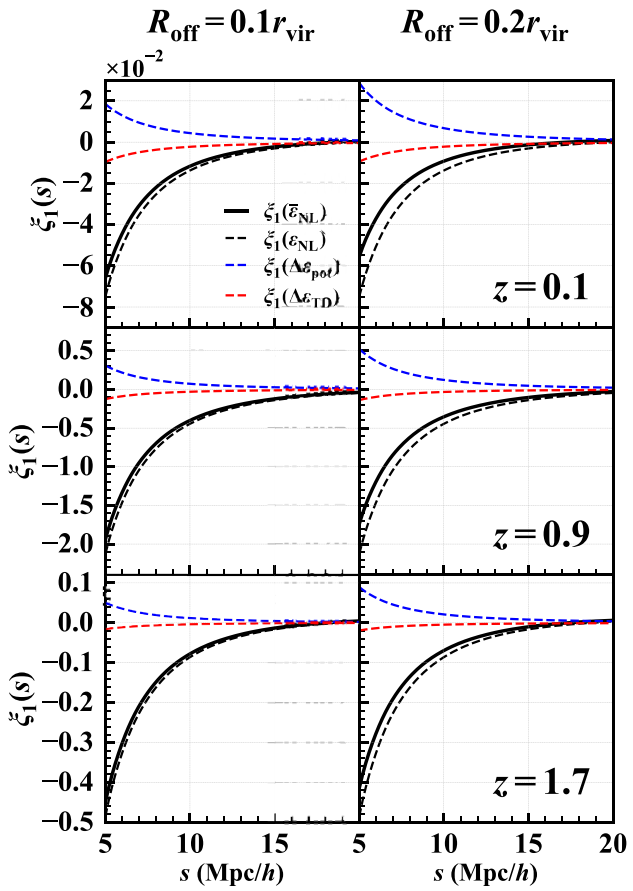

Figure 12. Impacts of the off-centred galaxies on the dipole cross-correlation function at $z = 0.1$, 0.9, and 1.7 (from top to bottom). The black-solid and black-dashed lines, respectively, represent the results including and neglecting the off-centring effects. The off-centred galaxies induce two effects: lowering the halo potential and introducing the virial motion which gives rise to the transverse Doppler effect. Contributions of these two effects are, respectively, shown in the blue ($\xi_1(\Delta\epsilon_{\rm pot})$, equation 48) and red ($\xi_1(\Delta\epsilon_{\rm TD})$, equation 49) dashed lines. The effects of the off-centred galaxies are characterized by the parameter $R_{\rm off}$ (see below equation 40). In the left-hand and right-hand panels, we set it to $R_{\rm off} = 0.2r_{\rm vir}$ and $R_{\rm off} = 0.1r_{\rm vir}$, respectively. The bias parameters are fixed to be $b_{\rm X} = 2.5$ and $b_{\rm Y} = 1.5$.

systematics arising from the off-centred galaxies lower the dipole signals. The fractional changes in dipole amplitude are typically 7–25 per cent at $s \lesssim 10$ Mpc h^{-1}. That is, the gravitational redshift effect still dominates the dipole signal at small scales.

To better understand the impact of the off-centring effects, we divide the expression of $\bar{\epsilon}_{\rm NL}$ into the three pieces as $\bar{\epsilon}_{\rm NL} = \epsilon_{\rm NL} + \Delta\epsilon_{\rm pot} + \Delta\epsilon_{\rm TD}$, where the last two terms represent, respectively, the diminution of the halo potential and the contribution from the transverse Doppler effect, defined by

$$\Delta\epsilon_{\rm pot} = -\frac{1}{aH}\left\{\bar{\phi}_{\rm NFW}(z, M, R_{\rm off}) - \phi_{\rm NFW,0}(z, M)\right\}, \quad (48)$$

$$\Delta\epsilon_{\rm TD} = \frac{1}{aH}\frac{1}{2}\bar{\sigma}_v^2(z, M, R_{\rm off}). \quad (49)$$

Since the model considered here involves the terms that is linearly proportional to $\epsilon_{\rm NL}$, the dipole signal taking the off-centring effects into account, $\xi_1(\bar{\epsilon}_{\rm NL})$, is decomposed into the three pieces:

$$\xi_1(\bar{\epsilon}_{\rm NL}) = \xi_1(\epsilon_{\rm NL}) + \xi_1(\Delta\epsilon_{\rm pot}) + \xi_1(\Delta\epsilon_{\rm TD}). \quad (50)$$

In Fig. 12, the two contributions $\xi_1(\Delta\epsilon_{\rm pot})$ and $\xi_1(\Delta\epsilon_{\rm TD})$ are, respectively, plotted in blue and red dashed lines. We find that these two contributions are competitive, and have different signs. That is, a small impact of the off-centring effects is partly ascribed to the cancellation between the two competitive effects. Note that the negative amplitude of the term $\xi_1(\Delta\epsilon_{\rm TD})$ comes from the fact that the velocity dispersion of galaxies, σ_v^2, is dominated by the virial motion inside the halo, and the dispersion $\sigma_{\rm vir}^2$ monotonically increases with the halo mass.[7] These trends would hold even if we consider a more elaborate estimation of the transverse Doppler effect, the cancellation of the off-centring effects is expected to still happen for more accurate modelling, and thus their impact on the dipole signal would be small.

6 SUMMARY AND PERSPECTIVES

It has been recognized that the observational relativistic effects, mainly arising from the light propagation in an inhomogeneous universe, induce the dipole asymmetry in the cross-correlation function between the haloes or galaxies having different clustering biases. In particular, the dipole asymmetry at small scales has been recently found to be dominated by the gravitational redshift effects (Breton et al. 2019; Saga et al. 2020). Thus, the detection of the dipole signal at small scales would provide an interesting opportunity for an alternative test of gravity. In this paper, we have studied analytically the future detectability of the dipole signal induced by the gravitational redshift effect.

In doing so, we have exploited a simple analytical description for the dipole cross-correlation function valid at quasi-linear regime. Previously, Saga et al. (2020) presented a quasi-linear model of the cross-correlation function. Taking the two major relativistic effects, i.e. the standard Doppler and gravitational redshift effects into account (but ignoring other minor contributions including magnification bias), we adopted the Zel'dovich approximation and halo model prescription to describe the dipole signals beyond the linear scales. While the quantitative model predictions successfully explain the dipole cross-correlation functions measured from the halo catalogues into which all possible relativistic effects arising from the light propagation are fully incorporated (Breton et al. 2019), the analytical model involves seven dimensional integrals, and the time-consuming numerical integration needs to be performed. To remedy this, in this paper, we derive new approximate expressions for the galaxy/halo density field based on the Lagrangian perturbative treatment, including also the halo model prediction to account for the non-perturbative potential contributions (see equations 14–17). These results enable us to obtain rather simplified analytical expression for the dipole cross-correlation function, and we found it to quantitatively reproduce the previous result of Saga et al. (2020) as well as the measured dipole signals in numerical simulations. The new analytical model of dipole cross-correlation function, presented in equations (23)–(25), involves only 1D integrals, and thus one can quickly predict the dipole signal, making the practical application of it to the Bayesian parameter estimation with Markov chain Monte Carlo technique possible.

Based on the new analytical model, we have computed analytically the covariance matrix of the dipole cross-correlation function, and

[7] If one considers the situation that the virial motion is ignorable, the sign of $\xi_1(\Delta\epsilon_{\rm TD})$ becomes positive. This is because the velocity dispersion $\sigma_v^2 \simeq \sigma_{\rm halo}^2$ now becomes a decreasing function of the halo mass. Such a situation has been considered in Breton et al. (2019), Kaiser (2013), Zhao et al. (2013).

investigated its behaviours. We found that the Gaussian covariance is mostly dominated by the two contributions, i.e. the term characterizing the cross-talk between the cosmic variance and Poisson noise, and the term purely originating from the Poisson shot noises, as similarly found by Hall & Bonvin (2017). As a result, the covariance matrix is shown to sensitively depend on not only the survey parameters (redshift depth and survey area of the galaxy surveys) but also the bias and number density of the galaxies/haloes to cross-correlate.

Plugging further the analytical predictions of both the dipole signal and covariance matrix into the definition of signal-to-noise ratio, we have quantitatively explored, in various setup for upcoming surveys, the feasibility to detect the dipole cross-correlation function, especially focusing on the scales where the gravitational redshift effect starts to be dominated and changes the sign of the dipole amplitudes. Our main findings are summarized as follows:

(i) In most of the cases we examined, the signal-to-noise ratio of the dipole cross-correlation functions becomes maximum around $z \approx 0.5$ (see Figs 6, 7, and 8). For the non-perturbative halo potential described by the NFW profile, the trend would generically appear true if one considers surveys with a fixed redshift interval in the universe close to the ΛCDM model.

(ii) Generally, cross-correlating between galaxies having large number densities with a larger difference of the clustering biases enhances the signal-to-noise ratio. Also, the signal-to-noise ratio becomes further increasing if the bias parameters for both of the galaxies gets large. For an idealistic situation with the galaxies of the number density $n_{\rm X,Y} \approx 10^{-3}\,({\rm Mpc}\,h^{-1})^{-3}$ and the biases $(b_{\rm X}, b_{\rm Y}) = (3.5, 1.5)$, it reaches $f_{\rm sky}^{-1/2}\,{\rm S/N} = 75.5$ for a survey at $z = 0.5$ with the interval of $\Delta z = 0.1$ (see Fig. 8).

(iii) For planned future galaxy surveys considered, if one divides the galaxy samples in each survey into two subsamples, a statistically significant detection of the dipole signal is expected from DESI-BGS, DESI-LRG, and SKA2 samples, and the signal-to-noise ratios of these samples reach 23, 11, and 13, respectively (see Fig. 10).

(iv) On the other hand, if the survey regions of the two different samples are overlapped, one can take a cross-correlation between them without dividing the samples into two. In this case, the dipole cross-correlation between DESI-LRG and SKA2 samples gives the largest signal-to-noise ratio, S/N ≈ 21. A solid detection of the dipole signal is also expected from the cross-correlations between DESI-LRG and DESI-ELG samples, and SKA2 and DESI-BGS samples, leading respectively to the signal-to-noise ratios, S/N = 11 and 16 (see Fig. 11).

(v) As possible systematic effects arising from the off-centred galaxies, the diminution of the gravitational redshift effect from the halo potential and the non-vanishing transverse Doppler effect can change the dipole signal at small scales. However, these two effects are found to be competitive, leading to different signs of the dipole cross-correlations (blue and red dashed lines in Fig. 12). As a result of the partial cancellation, the net result of their contributions becomes small, and the dipole signal at $s \lesssim 10\,{\rm Mpc}\,h^{-1}$ is shown to be still dominated by the gravitational redshift effect.

Our forecast study suggests that upcoming surveys enable us to detect dipole signals at a statistically significant level, and this would offer a unique probe of the depth of the halo gravitational potential. Exploiting the dipole to test the fundamental physics would be also an interesting subject through a precision measurement of the gravitational redshift effect, and this is left to our future work.

Note that the major findings summarized above rely on several assumptions and simplification based on the halo model. In particular, our analysis assumes the one-to-one correspondence between halo and galaxy distributions. For more realistic estimations, a proper account of the halo–galaxy connection would be crucial, using e.g. the halo-occupation distribution approach, in which the contribution of the so-called satellites would play a substantial role to detect the dipole signal. Furthermore, in this paper, the gravitational redshift effect from the halo potential is computed from the NFW profile, whose potential depth is solely determined by the halo mass and redshift for a given cosmological model. However, even for a fixed halo mass, halo clustering features have been known to depend on secondary halo properties that correlate with halo assembly history, referred to as the halo assembly bias (see e.g. Gao, Springel & White 2005; Zentner et al. 2005). This effect would give a systematic impact on the estimation of the halo potential, and proper modelling of it needs further study.

Finally, we have investigated the detectability of the dipole signal, restricting the scales to $s \geq 5\,{\rm Mpc}\,h^{-1}$, where our analytical prediction of the dipole cross-correlation is shown to reproduce quantitatively the simulation results well. Nevertheless, below this scale, the amplitude of the dipole cross-correlation is expected to become further large (with a negative sign), and thus the signal-to-noise ratio would be improved if one uses the cross-correlation data at small scales. In doing so, however, the analytical treatment based on perturbation theory may not be adequate, and one has to exploit a method to quantitatively predict the dipole cross-correlation function, taking consistently not only the non-linear gravitational clustering but also the baryonic effects on the galaxy distribution into account. This is a challenging task, but is worth for further investigation towards a decisive detection of the gravitational redshift effect.

ACKNOWLEDGEMENTS

This work was initiated during the invitation program of JSPS Grant No. L16519. Numerical simulation was granted access to HPC resources of TGCC through allocations made by GENCI (Grand Equipement National de Calcul Intensif) under the allocations A0030402287, A0050402287, A0070402287, and A0090402287. Numerical computation was also carried out partly at the Yukawa Institute Computer Facility. This work was supported by Grant-in-Aid for JSPS Fellows No. 17J10553 (SS) and in part by MEXT/JSPS KAKENHI Grant Numbers Nos. JP17H06359, JP20H05861, and 21H01081 (AT). AT also acknowledges the support from JST AIP Acceleration Research Grant No. JP20317829, Japan. The authors thank the Yukawa Institute for Theoretical Physics at Kyoto University. Discussions during the YITP workshop YITP-T-21-06 on 'Galaxy shape statistics and cosmology' were useful to complete this work.

DATA AVAILABILITY

The data underlying this article are available in RayGalGroupSims Relativistic Halo Catalogues at https://cosmo.obspm.fr/public-datasets/.

REFERENCES

Alam S. et al., 2017a, MNRAS, 470, 2617
Alam S., Zhu H., Croft R. A. C., Ho S., Giusarma E., Schneider D. P., 2017b, MNRAS, 470, 2822
Bardeen J. M., Bond J. R., Kaiser N., Szalay A. S., 1986, ApJ, 304, 15
Beutler F., Di Dio E., 2020, J. Cosmol. Astropart. Phys., 2020, 048
Bonvin C., Durrer R., 2011, Phys. Rev. D, 84, 063505
Bonvin C., Fleury P., 2018, J. Cosmol. Astropart. Phys., 2018, 061

Bonvin C., Hui L., Gaztañaga E., 2014, Phys. Rev. D, 89, 083535
Bonvin C., Hui L., Gaztanaga E., 2016, J. Cosmol. Astropart. Phys., 2016, 021
Bonvin C., Oliveira Franco F., Fleury P., 2020, J. Cosmol. Astropart. Phys., 2020, 004
Borzyszkowski M., Bertacca D., Porciani C., 2017, MNRAS, 471, 3899
Breton M.-A., Rasera Y., Taruya A., Lacombe O., Saga S., 2019, MNRAS, 483, 2671
Bull P., Camera S., Raccanelli A., Blake C., Ferreira P., Santos M., Schwarz D. J., 2015, in Proc. Sci., Advancing Astrophysics with the Square Kilometre Array. SISSA, Trieste, PoS#024
Bullock J. S., Kolatt T. S., Sigad Y., Somerville R. S., Kravtsov A. V., Klypin A. A., Primack J. R., Dekel A., 2001, MNRAS, 321, 559
Cai Y.-C., Kaiser N., Cole S., Frenk C., 2017, MNRAS, 468, 1981
Challinor A., Lewis A., 2011, Phys. Rev. D, 84, 043516
Coates L., Adamek J., Bull P., Guandalin C., Clarkson C., 2021, MNRAS, 504, 3534
Cohn J. D., 2006, New Astron., 11, 226
Cooray A., Sheth R., 2002, Phys. Rep., 372, 1
Croft R. A. C., 2013, MNRAS, 434, 3008
DESI Collaboration 2016, preprint (arXiv:1611.00036)
Di Dio E., Seljak U., 2019, J. Cosmol. Astropart. Phys., 2019, 050
Euclid Collaboration, 2020, A&A, 642, A191
Fisher K. B., Scharf C. A., Lahav O., 1994, MNRAS, 266, 219
Gao L., Springel V., White S. D. M., 2005, MNRAS, 363, L66
Grieb J. N., Sánchez A. G., Salazar-Albornoz S., Dalla Vecchia C., 2016, MNRAS, 457, 1577
Guandalin C., Adamek J., Bull P., Clarkson C., Abramo L. R., Coates L., 2021, MNRAS, 501, 2547
Guzzo L. et al., 2008, Nature, 451, 541
Hall A., Bonvin C., 2017, Phys. Rev. D, 95, 043530
Hamilton A. J. S., 1992, ApJ, 385, L5
Hamilton A. J. S., Culhane M., 1996, MNRAS, 278, 73
Hikage C., Mandelbaum R., Takada M., Spergel D. N., 2013, MNRAS, 435, 2345
Jimeno P., Broadhurst T., Coupon J., Umetsu K., Lazkoz R., 2015, MNRAS, 448, 1999
Kaiser N., 1987, MNRAS, 227, 1
Kaiser N., 2013, MNRAS, 435, 1278
Komatsu E. et al., 2011, ApJS, 192, 18
Laureijs R. et al., 2011, preprint (arXiv:1110.3193)
Lepori F., Di Dio E., Villa E., Viel M., 2018, J. Cosmol. Astropart. Phys., 2018, 043
Linder E. V., 2008, Astropart. Phys., 29, 336
Łokas E. L., Mamon G. A., 2001, MNRAS, 321, 155
Matsubara T., 2000, ApJ, 535, 1
Matsubara T., 2004, ApJ, 615, 573
McDonald P., 2009, J. Cosmol. Astropart. Phys., 2009, 026
Mpetha C. T. et al., 2021, MNRAS, 503, 669
Navarro J. F., Frenk C. S., White S. D. M., 1996, ApJ, 462, 563
Novikov E. A., 1969, Sov. J. Exp. Theoret. Phys., 30, 512
Pápai P., Szapudi I., 2008, MNRAS, 389, 292
Percival W. J., White M., 2009, MNRAS, 393, 297
Pyne T., Birkinshaw M., 2004, MNRAS, 348, 581
Reid B. A. et al., 2012, MNRAS, 426, 2719
Sadeh I., Feng L. L., Lahav O., 2015, Phys. Rev. Lett., 114, 071103
Saga S., Taruya A., Breton M.-A., Rasera Y., 2020, MNRAS, 498, 981
Sánchez A. G. et al., 2013, MNRAS, 433, 1202
Sasaki M., 1987, MNRAS, 228, 653
Shandarin S. F., Zeldovich Y. B., 1989, Rev. Mod. Phys., 61, 185
Sheth R. K., Diaferio A., 2001, MNRAS, 322, 901
Sheth R. K., Tormen G., 1999, MNRAS, 308, 119
Smith R. E., 2009, MNRAS, 400, 851
Square Kilometre Array Cosmology Science Working Group 2020, Publ. Astron. Soc. Austr., 37, e007
Szalay A. S., Matsubara T., Landy S. D., 1998, ApJ, 498, L1
Szapudi I., 2004, ApJ, 614, 51
Takada M. et al., 2014, PASJ, 66, R1
Tansella V., Bonvin C., Durrer R., Ghosh B., Sellentin E., 2018, J. Cosmol. Astropart. Phys., 2018, 019
Taruya A., Saga S., Breton M.-A., Rasera Y., Fujita T., 2020, MNRAS, 491, 4162
Tinker J., Kravtsov A. V., Klypin A., Abazajian K., Warren M., Yepes G., Gottlöber S., Holz D. E., 2008, ApJ, 688, 709
Tinker J. L., Robertson B. E., Kravtsov A. V., Klypin A., Warren M. S., Yepes G., Gottlöber S., 2010, ApJ, 724, 878
Wojtak R., Hansen S. H., Hjorth J., 2011, Nature, 477, 567
Yahya S., Bull P., Santos M. G., Silva M., Maartens R., Okouma P., Bassett B., 2015, MNRAS, 450, 2251
Yoo J., 2010, Phys. Rev. D, 82, 083508
Yoo J., 2014, Class. Quantum Gravity, 31, 234001
Yoo J., Fitzpatrick A. L., Zaldarriaga M., 2009, Phys. Rev. D, 80, 083514
Yoo J., Hamaus N., Seljak U., Zaldarriaga M., 2012, Phys. Rev. D, 86, 063514
Zaroubi S., Hoffman Y., 1996, ApJ, 462, 25
Zel'dovich Y. B., 1970, A&A, 5, 84
Zentner A. R., Berlind A. A., Bullock J. S., Kravtsov A. V., Wechsler R. H., 2005, ApJ, 624, 505
Zhao H., Peacock J. A., Li B., 2013, Phys. Rev. D, 88, 043013
Zhu H., Alam S., Croft R. A. C., Ho S., Giusarma E., 2017, MNRAS, 471, 2345

APPENDIX A: DERIVATIONS OF THE MULTIPOLE MOMENTS

In this appendix, we summarize key expressions to derive the dipole cross-correlation function presented in Section 2.2.

Based on the density fields given at equation (14) together with equations (15)–(17), let us first compute cross-correlation function. Substituting these equations into equation (19), we obtain

$$\xi_{\rm XY}^{\rm (std)} = \int \frac{{\rm d}^3k}{(2\pi)^3} {\rm e}^{{\rm i}\boldsymbol{k}\cdot\boldsymbol{s}} \left(b_{\rm X}^{\rm E} + f\mu_{k1}^2 + {\rm i}f\frac{2}{ks_1}\mu_{k1}\right) \times \left(b_{\rm Y}^{\rm E} + f\mu_{k2}^2 - {\rm i}f\frac{2}{ks_2}\mu_{k2}\right) P_{\rm L}(k), \tag{A1}$$

$$\xi_{\rm XY}^{\rm (pot)} = \int \frac{{\rm d}^3k}{(2\pi)^3} {\rm e}^{i\boldsymbol{k}\cdot\boldsymbol{s}} \left[\left(b_{\rm X}^{\rm E} + f\mu_{k1}^2 + {\rm i}f\frac{2}{ks_1}\mu_{k1}\right)\left({\rm i}k\mu_{k2} + \frac{2}{s_2}\right) + \left(b_{\rm Y}^{\rm E} + f\mu_{k2}^2 - {\rm i}f\frac{2}{ks_2}\mu_{k2}\right)\left(-{\rm i}k\mu_{k1} + \frac{2}{s_1}\right)\right]\frac{\mathcal{M}}{k^2}P_{\rm L}(k), \tag{A2}$$

$$\begin{aligned}\xi_{\rm XY}^{(\epsilon_{\rm NL})} = \int \frac{{\rm d}^3k}{(2\pi)^3} {\rm e}^{{\rm i}\boldsymbol{k}\cdot\boldsymbol{s}} \Bigg[& \frac{\epsilon_{\rm NL,X}}{s_1}\left(-1 + \mu_{k1}^2 + {\rm i}f\frac{2}{ks_1}\mu_{k1} + {\rm i}b_{\rm X}^{\rm E}ks_1\mu_{k1} - 2f\mu_{k1}^2 + {\rm i}\frac{2}{ks_1}\mu_{k1} + {\rm i}fks_1\mu_{k1}^3\right) \\ & \times \left(b_{\rm Y}^{\rm E} + f\mu_{k2}^2 - {\rm i}f\frac{2}{ks_2}\mu_{k2}\right) \\ & + \frac{\epsilon_{\rm NL,Y}}{s_2}\left(-1 + \mu_{k2}^2 - {\rm i}f\frac{2}{ks_2}\mu_{k2} - {\rm i}b_{\rm Y}^{\rm E}ks_2\mu_{k2} - 2f\mu_{k2}^2 - {\rm i}\frac{2}{ks_2}\mu_{k2} - {\rm i}fks_2\mu_{k2}^3\right) \\ & \times \left(b_{\rm X}^{\rm E} + f\mu_{k1}^2 + {\rm i}f\frac{2}{ks_1}\mu_{k1}\right)\Bigg] P_{\rm L}(k),\end{aligned} \tag{A3}$$

where we define $\mu_{k1} = \hat{\boldsymbol{s}}_1 \cdot \hat{\boldsymbol{k}}$ and $\mu_{k2} = \hat{\boldsymbol{s}}_2 \cdot \hat{\boldsymbol{k}}$. The function $P_{\rm L}(k)$ stands for the linear power spectrum of the density field $\delta_{\rm L}$ given by

$$\left\langle \delta_{\rm L}(\boldsymbol{k})\delta_{\rm L}(\boldsymbol{k}')\right\rangle = (2\pi)^3\delta_{\rm D}(\boldsymbol{k}+\boldsymbol{k}')P_{\rm L}(k). \tag{A4}$$

Equations (A1)–(A3) involve the 3D integrals over $\boldsymbol{k}$. Introducing the polar coordinate, the angular integral can be performed by using the following formulae:

$$\int \frac{\mathrm{d}\Omega_{\boldsymbol{k}}}{4\pi} e^{i\boldsymbol{k}\cdot\boldsymbol{s}} = j_0(ks), \tag{A5}$$

$$\int \frac{\mathrm{d}\Omega_{\boldsymbol{k}}}{4\pi} e^{i\boldsymbol{k}\cdot\boldsymbol{s}} \left(i\hat{k}_a\right) = -j_1(ks)\hat{s}_a, \tag{A6}$$

$$\int \frac{\mathrm{d}\Omega_{\boldsymbol{k}}}{4\pi} e^{i\boldsymbol{k}\cdot\boldsymbol{s}} \left(\hat{k}_a\hat{k}_b\right) = -j_2(ks)\hat{s}_a\hat{s}_b + \frac{j_1(ks)}{ks}\delta_{ab}, \tag{A7}$$

$$\int \frac{\mathrm{d}\Omega_{\boldsymbol{k}}}{4\pi} e^{i\boldsymbol{k}\cdot\boldsymbol{s}} \left(i\hat{k}_a\hat{k}_b\hat{k}_c\right) = j_3(ks)\hat{s}_a\hat{s}_b\hat{s}_c - \frac{j_2(ks)}{ks}(\hat{s}_a\delta_{bc} + \hat{s}_b\delta_{ca} + \hat{s}_c\delta_{ab}), \tag{A8}$$

$$\int \frac{\mathrm{d}\Omega_{\boldsymbol{k}}}{4\pi} e^{i\boldsymbol{k}\cdot\boldsymbol{s}} \left(\hat{k}_a\hat{k}_b\hat{k}_c\hat{k}_d\right) = j_4(ks)\hat{s}_a\hat{s}_b\hat{s}_c\hat{s}_d - \frac{j_3(ks)}{ks}(\hat{s}_a\hat{s}_b\delta_{cd} + \hat{s}_b\hat{s}_c\delta_{ad} + \hat{s}_b\hat{s}_d\delta_{ac} + \hat{s}_a\hat{s}_c\delta_{bd} + \hat{s}_a\hat{s}_d\delta_{bc} + \hat{s}_c\hat{s}_d\delta_{ab}) + \frac{j_2(ks)}{(ks)^2}(\delta_{ad}\delta_{bc} + \delta_{ac}\delta_{bd} + \delta_{ab}\delta_{cd}), \tag{A9}$$

$$\int \frac{\mathrm{d}\Omega_{\boldsymbol{k}}}{4\pi} e^{i\boldsymbol{k}\cdot\boldsymbol{s}} \left(i\hat{k}_a\hat{k}_b\hat{k}_c\hat{k}_d\hat{k}_e\right) = -j_5(ks)\hat{s}_a\hat{s}_b\hat{s}_c\hat{s}_d\hat{s}_e + \frac{j_{4(ks)}}{ks}(\hat{s}_a\hat{s}_b\hat{s}_c\delta_{de} + 9\ \text{perm.}) - \frac{j_{3(ks)}}{(ks)^2}(\hat{s}_a\delta_{bc}\delta_{de} + 14\ \text{perm.}), \tag{A10}$$

where j_ℓ stands for the spherical Bessel function.

As a result of the angular integration, the dependence of the correlation function on the vectors $\boldsymbol{s}_1$ and $\boldsymbol{s}_2$ in equations (A1)–(A3) is shown to be described by the following quantities: $(\hat{\boldsymbol{s}}\cdot\hat{\boldsymbol{s}}_1)$, $(\hat{\boldsymbol{s}}\cdot\hat{\boldsymbol{s}}_2)$, $(\hat{\boldsymbol{s}}_1\cdot\hat{\boldsymbol{s}}_2)$, s_1, and s_2. Note that these are re-expressed in terms of the three variables, i.e. separation $s = |\boldsymbol{s}_2 - \boldsymbol{s}_1|$, the line-of-sight distance $d = |\boldsymbol{s}_1 + \boldsymbol{s}_2|/2$, and directional cosine $\mu = \hat{\boldsymbol{s}}\cdot\hat{\boldsymbol{d}}$. Since we are interested in the cases with $s \ll d$, one can expand the quantities as

$$s_1 = d\left(1 - \frac{s}{d}\mu + \frac{1}{4}\left(\frac{s}{d}\right)^2\right)^{1/2} \simeq d\left(1 - \frac{1}{2}\frac{s}{d}\mu\right), \tag{A11}$$

$$s_2 = d\left(1 + \frac{s}{d}\mu + \frac{1}{4}\left(\frac{s}{d}\right)^2\right)^{1/2} \simeq d\left(1 + \frac{1}{2}\frac{s}{d}\mu\right), \tag{A12}$$

$$(\hat{\boldsymbol{s}}\cdot\hat{\boldsymbol{s}}_1) = \frac{\mu - \frac{1}{2}\frac{s}{d}}{\left(1 - \frac{s}{d}\mu + \frac{1}{4}\left(\frac{s}{d}\right)^2\right)^{1/2}} \simeq \mu - \frac{1}{2}(1-\mu^2)\frac{s}{d}, \tag{A13}$$

$$(\hat{\boldsymbol{s}}\cdot\hat{\boldsymbol{s}}_2) = \frac{\mu + \frac{1}{2}\frac{s}{d}}{\left(1 + \frac{s}{d}\mu + \frac{1}{4}\left(\frac{s}{d}\right)^2\right)^{1/2}} \simeq \mu + \frac{1}{2}(1-\mu^2)\frac{s}{d}, \tag{A14}$$

$$(\hat{\boldsymbol{s}}_1\cdot\hat{\boldsymbol{s}}_2) = \frac{1 - \frac{1}{4}\left(\frac{s}{d}\right)^2}{\left(1 - \frac{s}{d}\mu + \frac{1}{4}\left(\frac{s}{d}\right)^2\right)^{1/2}\left(1 + \frac{s}{d}\mu + \frac{1}{4}\left(\frac{s}{d}\right)^2\right)^{1/2}} \simeq 1, \tag{A15}$$

where the last equalities in each equation is valid at $\mathcal{O}(s/d)$. Substituting these expressions into the cross-correlation function, the results are divided into the plane-parallel ($d \to \infty$) and leading-order wide-angle contributions ($O(s/d)$), in which the dependence of the directional cosine is factorized, and is expressed as a polynomial form of μ. Thus, applying the multipole expansion, one easily derives the analytical expression for the multipole correlation functions, summarized in Appendix C.

APPENDIX B: COMPARISON WITH APPROXIMATE FORMULA IN SAGA ET AL. (2020)

Employing the Zel'dovich approximation and combining the non-perturbative contribution from the halo potential, Saga et al. (2020) have built a quasi-linear model of the dipole cross-correlation function, which successfully explains numerical simulations at both small and large scales. While a rigorous treatment of their model requires the time-consuming multidimensional integration, they also derived a simple approximate expression for the dipole moment, which resembles the analytical model presented in this paper. In this appendix, we clarify the similarity and difference between the approximate expression derived in Section 2.1 and the one obtained from Saga et al. (2020) (see their equation (4.2) in Section 4.2).

In Saga et al. (2020), the simplified expression of the dipole was derived based on a perturbative treatment of their rigorous quasi-linear model. Ignoring the non-perturbative halo potential, let us first denote the cross-correlation function of their model by $\xi_{\mathrm{XY},\epsilon_{\mathrm{NL}}=0}(\boldsymbol{s}_1,\boldsymbol{s}_2)$. We then consider the gravitational redshift contributions arising from the non-perturbative halo potential, which gives a systematic offset of the redshift-space positions away from the observer (origin), i.e. $\boldsymbol{s}_{1,2} \to \boldsymbol{s}_{1,2} - \epsilon_{\mathrm{NL,X/Y}}\hat{\boldsymbol{s}}_{1,2}$. The resultant cross-correlation function taking the halo potential into account, ξ_{XY}, is expressed as

$$\begin{aligned}\xi_{\mathrm{XY}}(\boldsymbol{s}_1,\boldsymbol{s}_2) &= \xi_{\mathrm{XY},\epsilon_{\mathrm{NL}}=0}\left(\boldsymbol{s}_1 - \epsilon_{\mathrm{NL,X}}\hat{\boldsymbol{s}}_1,\ \boldsymbol{s}_2 - \epsilon_{\mathrm{NL,Y}}\hat{\boldsymbol{s}}_2\right)\\ &\simeq \left[1 - \left\{\epsilon_{\mathrm{NL,X}}\,\hat{\boldsymbol{s}}_1\cdot\boldsymbol{\nabla}_{s_1} + \epsilon_{\mathrm{NL,Y}}\,\hat{\boldsymbol{s}}_2\cdot\boldsymbol{\nabla}_{s_2}\right\}\right]\\ &\quad\times\xi_{\mathrm{XY},\epsilon_{\mathrm{NL}}=0}(\boldsymbol{s}_1,\boldsymbol{s}_2).\end{aligned} \tag{B1}$$

Here, in the second equality, the systematic offset caused by the halo potential is treated as a small perturbation and is expanded at linear order, as similarly done by Saga et al. (2020).

Note that expanding the displacement field $\boldsymbol{\Psi}$ from the exponent and truncating it at linear order, the cross-correlation function $\xi_{\mathrm{XY},\epsilon_{\mathrm{NL}}=0}$ is shown to be identical to the cross-correlation function $\xi^{(\mathrm{std})}_{\mathrm{XY}} + \xi^{(\mathrm{pot})}_{\mathrm{XY}}$ given in this paper (see equation 19). With this linearized treatment, the above expression is reduced to

$$\begin{aligned}\xi_{\mathrm{XY}}(\boldsymbol{s}_1,\boldsymbol{s}_2) &\simeq \xi^{(\mathrm{std})}_{\mathrm{XY}}(\boldsymbol{s}_1,\boldsymbol{s}_2) + \xi^{(\mathrm{pot})}_{\mathrm{XY}}(\boldsymbol{s}_1,\boldsymbol{s}_2)\\ &\quad - \left[\epsilon_{\mathrm{NL,X}}\,\hat{\boldsymbol{s}}_1\cdot\boldsymbol{\nabla}_{s_1} + \epsilon_{\mathrm{NL,Y}}\,\hat{\boldsymbol{s}}_2\cdot\boldsymbol{\nabla}_{s_2}\right]\xi^{(\mathrm{std})}_{\mathrm{XY}}(\boldsymbol{s}_1,\boldsymbol{s}_2)\\ &\equiv \xi^{(\mathrm{std})}_{\mathrm{XY}}(\boldsymbol{s}_1,\boldsymbol{s}_2) + \xi^{(\mathrm{pot})}_{\mathrm{XY}}(\boldsymbol{s}_1,\boldsymbol{s}_2) + \widetilde{\xi}^{(\epsilon_{\mathrm{NL}})}_{\mathrm{XY}}(\boldsymbol{s}_1,\boldsymbol{s}_2),\end{aligned} \tag{B2}$$

where, in the first equality, we used the fact that the term $\xi^{(\mathrm{pot})}_{\mathrm{XY}}$ only gives a sub-dominant contribution, and the contribution proportional to $\epsilon_{\mathrm{NL,X/Y}}\,\xi^{(\mathrm{pot})}_{\mathrm{XY}}$ have been ignored from the second line. The function $\widetilde{\xi}^{(\epsilon_{\mathrm{NL}})}_{\mathrm{XY}}(\boldsymbol{s}_1,\boldsymbol{s}_2)$ is explicitly given by

$$\begin{aligned}\widetilde{\xi}^{(\epsilon_{\mathrm{NL}})}_{\mathrm{XY}}(\boldsymbol{s}_1,\boldsymbol{s}_2) &= \frac{\epsilon_{\mathrm{NL,X}}}{s_1}\int\frac{\mathrm{d}^3\boldsymbol{k}}{(2\pi)^3}\,\mathrm{e}^{\mathrm{i}\boldsymbol{k}\cdot\boldsymbol{s}}\left(b_{\mathrm{Y}} + f\mu_{k2}^2 - \mathrm{i}\frac{2f}{ks_2}\mu_{k2}\right)\\ &\quad\times\left[(\mathrm{i}ks_1\mu_{k1})\left(b_{\mathrm{X}} + f\mu_{k1}^2 + \mathrm{i}\frac{2f}{ks_1}\mu_{k1}\right) + \mathrm{i}\frac{2f}{ks_1}\mu_{k1}\right]P_{\mathrm{L}}(k)\\ &\quad + (\mathrm{X}\leftrightarrow\mathrm{Y},\ s_1\leftrightarrow s_2,\ \mu_1\leftrightarrow-\mu_2).\end{aligned} \tag{B3}$$

Thus, comparing equation (B2) with the analytical model in Section 2.1, the difference essentially appears at the gravitational redshift contribution from the halo potential, i.e. $\widetilde{\xi}^{(\epsilon_{\mathrm{NL}})}_{\mathrm{XY}}$ and $\xi^{(\epsilon_{\mathrm{NL}})}_{\mathrm{XY}}$.

Taking their difference gives

$$\xi_{\rm XY}^{(\epsilon_{\rm NL})} - \widetilde{\xi}_{\rm XY}^{(\epsilon_{\rm NL})} = \frac{\epsilon_{\rm NL,X}}{s_1}\int\frac{{\rm d}^3\boldsymbol{k}}{(2\pi)^3}{\rm e}^{{\rm i}\boldsymbol{k}\cdot\boldsymbol{s}}\left(b_{\rm Y}+f\mu_{k2}^2-{\rm i}f\frac{2}{ks_2}\mu_{k2}\right)\times\left(-1+\mu_{k1}^2+{\rm i}f\frac{2}{ks_1}\mu_{k1}\right)P_{\rm L}(k)+({\rm X}\leftrightarrow{\rm Y},\ s_1\leftrightarrow s_2,\ \mu_1\leftrightarrow-\mu_2). \tag{B4}$$

As explicitly demonstrated in Fig. 2, this produces a rather small difference, and the simple approximation presented in Saga et al. (2020) leads to the prediction of the dipole moment almost identical to the one from the present analytical model.

APPENDIX C: MULTIPOLE COEFFICIENTS

Here, we present the analytical expressions for the multipole moments of the cross-correlation functions. As we discussed in previous Appendix and Section 2.2, the correlation function can be written as a function of the separation $s = |\boldsymbol{s}_2 - \boldsymbol{s}_1|$, line-of-sight distance $d = |(\boldsymbol{s}_1 + \boldsymbol{s}_2)/2|$, and directional cosine between the line-of-sight and separation vectors, given by $\mu = \hat{\boldsymbol{s}}\cdot\hat{\boldsymbol{d}}$. Based on the results in Appendix A, the cross-correlation function can be expanded in powers of (s/d). Further applying the multipole expansion, we obtain:

$$\xi_{\rm XY}(s,d,\mu) = \sum_\ell \xi_{{\rm XY},\ell}(s,d)\mathcal{L}_\ell(\mu) \tag{C1}$$

$$= \sum_\ell\left[\xi_{{\rm pp},\ell}(s)+\left(\frac{s}{d}\right)\xi_{{\rm wa},\ell}(s)+O\left(\left(\frac{s}{d}\right)^2\right)\right]\mathcal{L}_\ell(\mu), \tag{C2}$$

where the functions $\xi_{{\rm pp},\ell}(s)$ and $\xi_{{\rm wa},\ell}(s)$, respectively, represent the contribution in the plane-parallel limit and wide-angle correction at leading order. These expressions involve only the 1D integral given by

$$\xi_{{\rm pp},\ell}(s) = (-{\rm i})^\ell\int\frac{k^2\,{\rm d}k}{2\pi^2}P_{{\rm pp},\ell}(k,z)j_\ell(ks), \tag{C3}$$

$$\xi_{{\rm wa},\ell}(s) = (-{\rm i})^\ell\int\frac{k^2\,{\rm d}k}{2\pi^2}P_{{\rm wa},\ell}(k,z). \tag{C4}$$

Below, we separately present the analytical expressions for the functions $P_{{\rm pp},\ell}$ and $P_{{\rm wa},\ell}$. While we focus on the dipole moment ($\ell = 1$) in the main text, we summarize all the non-vanishing moments valid at the order of $\mathcal{O}(s/d)$.

C1 Plane-parallel limit

The non-vanishing multipoles in the plane-parallel limit are summarized as follows:

$$P_{{\rm pp},0}^{\rm (std)} = \left[b_{\rm X}b_{\rm Y}+\frac{1}{3}(b_{\rm X}+b_{\rm Y})f+\frac{1}{5}f^2\right]P_{\rm L}(k), \tag{C5}$$

$$P_{{\rm pp},2}^{\rm (std)} = \left[\frac{2}{3}f(b_{\rm X}+b_{\rm Y})+\frac{4}{7}f^2\right]P_{\rm L}(k), \tag{C6}$$

$$P_{{\rm pp},4}^{\rm (std)} = \left[\frac{8}{35}f^2\right]P_{\rm L}(k), \tag{C7}$$

for the standard Doppler contribution,

$$P_{{\rm pp},1}^{\rm (pot)} = \left[-{\rm i}(b_{\rm X}-b_{\rm Y})\frac{\mathcal{M}}{k}\right]P_{\rm L}(k), \tag{C8}$$

for the linear gravitational redshift contribution, and

$$P_{{\rm pp},1}^{(\epsilon_{\rm NL})} = \left[-{\rm i}(\epsilon_{\rm NL,X}-\epsilon_{\rm NL,Y})\left(b_{\rm X}b_{\rm Y}+\frac{3}{5}(b_{\rm X}+b_{\rm Y})f+\frac{3}{7}f^2\right)k\right]P_{\rm L}(k), \tag{C9}$$

$$P_{{\rm pp},3}^{(\epsilon_{\rm NL})} = \left[-{\rm i}(\epsilon_{\rm NL,X}-\epsilon_{\rm NL,Y})\frac{2}{45}f\,(9(b_{\rm X}+b_{\rm Y})+10f)k\right]P_{\rm L}(k), \tag{C10}$$

$$P_{{\rm pp},5}^{(\epsilon_{\rm NL})} = \left[-{\rm i}\frac{8}{63}f^2(\epsilon_{\rm NL,X}-\epsilon_{\rm NL,Y})k\right]P_{\rm L}(k), \tag{C11}$$

for the contribution arising from the non-perturbative halo potential.

C2 Wide-angle correction

The non-vanishing multipoles of the wide-angle correction are summarized as follows:

$$P_{{\rm wa},1}^{\rm (std)} = {\rm i}2f(b_{\rm X}-b_{\rm Y})\left[-\frac{1}{5}j_2(ks)+\frac{j_1(ks)}{ks}\right]P_{\rm L}(k), \tag{C12}$$

$$P_{{\rm wa},3}^{\rm (std)} = \left[-{\rm i}\frac{2f}{5}(b_{\rm X}-b_{\rm Y})j_2(ks)\right]P_{\rm L}(k). \tag{C13}$$

for the standard Doppler contribution,

$$P_{{\rm wa},0}^{\rm (pot)} = \frac{\mathcal{M}}{k}\left[-\frac{1}{3}\left(b_{\rm X}+b_{\rm Y}-\frac{2f}{5}\right)j_1(ks)+2(b_{\rm X}+b_{\rm Y})\frac{j_0(ks)}{ks}\right]P_{\rm L}(k), \tag{C14}$$

$$P_{{\rm wa},2}^{\rm (pot)} = \frac{\mathcal{M}}{k}\left[-\frac{1}{3}\left(b_{\rm X}+b_{\rm Y}-\frac{2}{5}f\right)j_1(ks)+\frac{8f}{35}j_3(ks)\right]P_{\rm L}(k), \tag{C15}$$

$$P_{{\rm wa},4}^{\rm (pot)} = \left[\frac{8}{35}\frac{\mathcal{M}f}{k}j_3(ks)\right]P_{\rm L}(k). \tag{C16}$$

for the linear gravitational redshift contribution, and

$$P_{{\rm wa},0}^{(\epsilon_{\rm NL})} = \left[\left\{-\frac{2f^2}{5}-\frac{2}{3}b_{\rm Y}-\frac{2f}{15}(1+5b_{\rm Y})\right\}ks\,j_{-1}(ks)+\left\{-\frac{13f^2}{35}-\frac{f}{15}(2+b_{\rm X}+7b_{\rm Y})+\frac{1}{3}(b_{\rm X}-2)b_{\rm Y}\right\}ks\,j_1(ks)+\frac{2f}{15}\left(5b_{\rm X}+3f\right)j_0(ks)\right]\frac{\epsilon_{\rm NL,X}}{s}\times P_{\rm L}(k)+({\rm X}\leftrightarrow{\rm Y}), \tag{C17}$$

$$P_{{\rm wa},2}^{(\epsilon_{\rm NL})} = \left[-\frac{1}{5}\left\{f^2+\frac{f}{21}(2+7b_{\rm X}+7b_{\rm Y})-\frac{1}{3}(2+5b_{\rm X})b_{\rm Y}\right\}ksj_1(ks)-\frac{1}{15}\left\{\frac{16f^2}{7}-2b_{\rm Y}+\frac{2f}{7}(1+6b_{\rm X}-4b_{\rm Y})\right\}ksj_3(ks)+\frac{4f}{21}(7b_{\rm X}+6f)j_2(ks)\right]\frac{\epsilon_{\rm NL,X}}{s}P_{\rm L}(k)+({\rm X}\leftrightarrow{\rm Y}), \tag{C18}$$

$$P^{(\epsilon_{\rm NL})}_{{\rm wa},4} = \left[\frac{4}{315} f(2-9b_{\rm X}+27b_{\rm Y}+2f)ksj_3(ks) + \frac{8f}{3465}(11-7f)ksj_5(ks)\right]\frac{\epsilon_{\rm NL,X}}{s}P_{\rm L}(k) + ({\rm X}\leftrightarrow{\rm Y}), \quad \text{(C19)}$$

$$P^{(\epsilon_{\rm NL})}_{{\rm wa},6} = \left[\frac{8}{231} f^2 ksj_5(ks) + \frac{16f^2}{35} j_4(ks)\right]\frac{\epsilon_{\rm NL,X}}{s}P_{\rm L}(k) + ({\rm X}\leftrightarrow{\rm Y}). \quad \text{(C20)}$$

for the non-perturbative contribution.

APPENDIX D: ON THE IMPACT OF THE MAGNIFICATION BIAS

In this appendix, we discuss the impact of the magnification bias on the dipole signal. In general, flux-limited galaxy samples inherently lead to the apparent density fluctuations through the fluctuation in luminosity distance, referred to as the magnification bias, which also induces the additional dipole signal beyond the plane-parallel limit (Bonvin & Durrer 2011; Hall & Bonvin 2017). The magnification bias mainly comes from two contributions: one is the lensing magnification and another is the Doppler magnification, among which the latter has been shown to produce a larger dipole signal (Hall & Bonvin 2017). At linear order, the Doppler magnification modulates the standard Doppler term. To be precise, the factor of $2/s$ in the last term at equation (15) is changed to $2/s \rightarrow 5s_{\rm B}aH + (2-5s_{\rm B})/s$, where the quantity $s_{\rm B}$ is the slope of the luminosity function (e.g. Bonvin & Durrer 2011; Hall & Bonvin 2017). Here, incorporating these contributions into our analytical model, we estimate the impact of the Doppler magnification on the dipole signal.

Coupling with other terms in the density field, the modulation due to the Doppler magnification mentioned above yields the following new contributions to the dipole cross-correlation (see equation 19):

$$\Delta\xi^{\rm (std)}_{{\rm XY},1} = \left(\frac{s}{d}\right)(1-aHd)f \times (5b_{\rm Y}s_{\rm B,X} - 5b_{\rm X}s_{\rm B,Y} + 3f(s_{\rm B,X}-s_{\rm B,Y}))\Xi^{(1)}_1, \quad \text{(D1)}$$

$$\Delta\xi^{\rm (pot)}_{{\rm XY},1} = -\left(\frac{s}{d}\right)10aHf\mathcal{M}s^2(s_{\rm B,X}-s_{\rm B,Y})\left(\Xi^{(0)}_0+\Xi^{(0)}_2\right), \quad \text{(D2)}$$

$$\Delta\xi^{(\epsilon_{\rm NL})}_{{\rm XY},1} = -\left(\frac{s}{d}\right)\frac{2aHf}{7}(s_{\rm B,Y}\epsilon_{\rm NL,X} - s_{\rm B,X}\epsilon_{\rm NL,Y}) \times \left(3f\Xi^{(0)}_0 + (7+12f)\Xi^{(1)}_1\right). \quad \text{(D3)}$$

In the above, all the corrections are found to be proportional to the factor (s/d), thus implying that these corrections are insignificant at small separation or higher redshift.

Using the expressions at equations (D1)–(D3), we show in Fig. D1 the impact of the Doppler magnification on the dipole signal, focusing particularly on small scales where the gravitational redshift effect becomes dominant. Here, we adopt the same parameter set as used in Fig. 12, but for the slope of the luminosity function, we set $s_{\rm B,X} = 1.2$ and $s_{\rm B,X} = 1.0$ that are the typical values for the LRG and ELG samples (e.g. Hall & Bonvin 2017). Fig. D1 shows that the Doppler magnification can contribute about 10 per cent to the dipole signal at low redshift, $z = 0.1$. On the other hand, going to higher redshifts, the contribution from the magnification bias becomes negligibly smaller, as we expected. Thus, we conclude that the impact of the Doppler magnification on the dipole signal is neglected as long as we consider the high redshifts and small scales, where the gravitational redshift effect dominates the dipole signal.

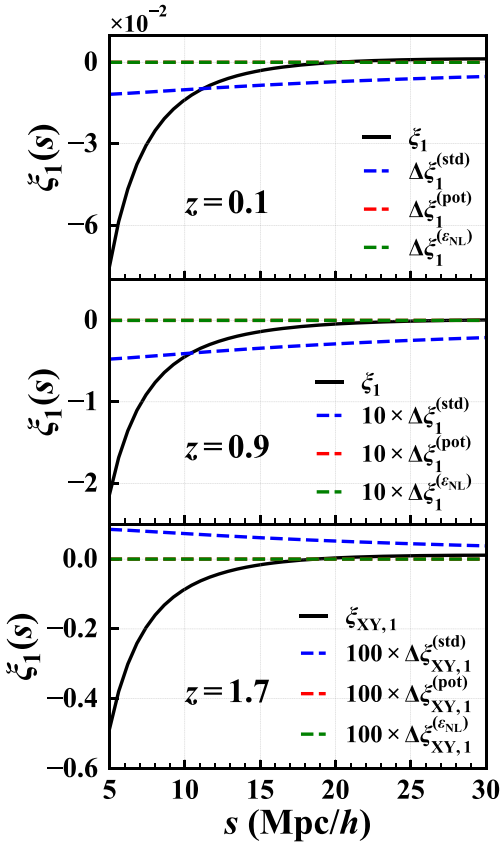

Figure D1. Impact of the magnification bias on the dipole moment from $z = 0.1$ (top) to 1.7 (bottom), given by equations (D1)–(D3). The parameters including the bias are the same as Fig. 12. We set the slope of the luminosity function as representative values of LRG and ELG for $s_{\rm B,X} = 1.2$ and $s_{\rm B,X} = 1.0$, respectively (Hall & Bonvin 2017). As seen in these figures, the magnification bias has less contribution to the dipole, especially at high redshift.

APPENDIX E: SURVEY PARAMETERS AND TARGET SAMPLES

In Section 4.3, we examine the detectability for the dipole in future surveys: DESI, *Euclid*, Subaru-PFS, and SKA. In this appendix, we summarize the survey parameters of each observation we used.

E1 Survey parameters and target samples

When calculating the signal-to-noise ratio, we use the values of the central redshift, width of redshift bins, number density, bias, and the fractional sky coverage or survey volume, for each survey. These survey parameters are summarized in Tables E1 (DESI-BGS), E2 (DESI-LRG/ELG), E3 (*Euclid*), E4 (Subaru-PFS), E5 (SKA1), and E6 (SKA2). In these tables, we also include the ratio of the number densities $n_{\rm X}(M_*)/n$ when the signal-to-noise ratio reaches its maximum (see Section 4.3 in detail). This will give us a guideline for future observations when we divide the sample into two subsamples.

Given the number density per unit redshift per square degree, $\mathrm{d}^2N/(\mathrm{d}z\,\mathrm{ddeg}^2)$, in order to obtain the number density per unit

Table E1. DESI Bright Galaxy Survey (BGS) (taken from table 2.5 of DESI Collaboration 2016). The bias of BLG in DESI Collaboration (2016) is assumed to be $b_{\rm BGS}(z) = 1.34/D_+(z)$. The width of the redshift bin and fractional sky coverage are, respectively, $\Delta z = 0.1$ and $f_{\rm sky} = 0.339$.

z	$n\,({\rm Mpc}\,h^{-1})^{-3}$	$n_{\rm X}(M_*)/n$
0.05	4.1×10^{-2}	6.6×10^{-3}
0.15	1.9×10^{-2}	7.4×10^{-3}
0.25	4.6×10^{-3}	8.3×10^{-3}
0.35	9.9×10^{-4}	9.4×10^{-3}
0.45	1.1×10^{-4}	1.1×10^{-2}

Table E2. DESI Luminous Red Galaxies (LRG) and Emission Line Galaxies (ELG) (taken from table 2.3 of DESI Collaboration 2016). The biases of LRG and ELG in DESI Collaboration (2016) are assumed to be $b_{\rm LRG}(z) = 1.7/D_+(z)$ and $b_{\rm ELG}(z) = 0.84/D_+(z)$, respectively. The width of the redshift bin and fractional sky coverage are, respectively, $\Delta z = 0.1$ and $f_{\rm sky} = 0.339$.

	ELG		LRG	
z	$n\,({\rm Mpc}\,h^{-1})^{-3}$	$n_{\rm X}(M_*)/n$	$n\,({\rm Mpc}\,h^{-1})^{-3}$	$n_{\rm X}(M_*)/n$
0.65	1.6×10^{-4}	1.8×10^{-3}	4.4×10^{-4}	2.3×10^{-2}
0.75	1.0×10^{-3}	2.3×10^{-3}	4.2×10^{-4}	2.6×10^{-2}
0.85	7.4×10^{-4}	2.8×10^{-3}	2.5×10^{-4}	2.2×10^{-2}
0.95	7.2×10^{-4}	2.3×10^{-3}	9.3×10^{-5}	2.6×10^{-2}
1.05	4.5×10^{-4}	2.9×10^{-3}	1.6×10^{-5}	2.3×10^{-2}
1.15	3.9×10^{-4}	3.6×10^{-3}	4.9×10^{-6}	2.7×10^{-2}
1.25	3.6×10^{-4}	3.1×10^{-3}	–	–
1.35	1.3×10^{-4}	3.9×10^{-3}	–	–
1.45	1.1×10^{-4}	3.4×10^{-3}	–	–
1.55	7.7×10^{-5}	4.4×10^{-3}	–	–
1.65	2.9×10^{-5}	5.6×10^{-3}	–	–

Table E3. Euclid with the fractional sky coverage $f_{\rm sky} = 0.364$, Hα Emission Line Galaxies (taken from table 3 of Euclid Collaboration 2019).

z	Δz	$n\,({\rm Mpc}\,h^{-1})^{-3}$	bias	$n_{\rm X}(M_*)/n$
1.0	0.2	6.86×10^{-4}	1.46	4.5×10^{-3}
1.2	0.2	5.58×10^{-4}	1.61	4.8×10^{-3}
1.4	0.2	4.21×10^{-4}	1.75	7.4×10^{-3}
1.65	0.3	2.61×10^{-4}	1.90	7.8×10^{-3}

Table E4. Subaru PFS with the fractional sky coverage $f_{\rm sky} = 0.0355$, [O II] Emission Line Galaxies (taken from table 2 of Takada et al. 2014).

z	Δz	$n\,({\rm Mpc}\,h^{-1})^{-3}$	bias	$n_{\rm X}(M_*)/n$
0.7	0.2	1.9×10^{-4}	1.18	1.7×10^{-3}
0.9	0.2	6.0×10^{-4}	1.26	2.5×10^{-3}
1.1	0.2	5.8×10^{-4}	1.34	2.7×10^{-3}
1.3	0.2	7.8×10^{-4}	1.42	2.9×10^{-3}
1.5	0.2	5.5×10^{-4}	1.50	3.2×10^{-3}
1.8	0.4	3.1×10^{-4}	1.62	3.3×10^{-3}
2.2	0.4	2.7×10^{-4}	1.78	3.1×10^{-3}

volume, n, we use the relation:

$$n = \frac{{\rm d}^2 N}{{\rm d}z\,{\rm ddeg}^2} \times \frac{\Delta z\, f_{\rm sky}}{V}, \tag{E1}$$

where the quantities $\Delta z, f_{\rm sky}$, and V are the width of the redshift bin, the fractional sky coverage, and survey volume, respectively.

Table E5. SKA1-MID with the fractional sky coverage $f_{\rm sky} = 0.121$ and the width of redshift bin $\Delta z = 0.1$, H I Galaxies (taken from table 1 of Bull et al. 2015). Only in the lowest redshift $z = 0.05$, since the given bias parameter is too small, equation (39) does not have a solution $M_{\rm min}$. Therefore, we will fix $M_{\rm min} = 10^8\,M_\odot\,h^{-1}$ only for this case, based on Yahya et al. (2015).

z	$n\,({\rm Mpc}^{-3})$	bias	$n_{\rm X}(M_*)/n$
0.05	2.92×10^{-2}	0.678	3.7×10^{-2}
0.15	6.74×10^{-3}	0.727	8.2×10^{-6}
0.25	1.71×10^{-3}	0.802	8.1×10^{-5}
0.35	4.64×10^{-4}	0.886	3.5×10^{-4}
0.45	1.36×10^{-4}	0.975	7.6×10^{-4}

Table E6. SKA2 with sky coverage with the fractional sky coverage $f_{\rm sky} = 0.727$ and the width of redshift bin $\Delta z = 0.1$, H I Galaxies (taken from table 1 of Bull et al. 2015).

z	$n\,({\rm Mpc}^{-3})$	bias	$n_{\rm X}(M_*)/n$
0.23	4.43×10^{-2}	0.713	2.0×10^{-6}
0.33	2.73×10^{-2}	0.772	4.6×10^{-5}
0.43	1.65×10^{-2}	0.837	1.5×10^{-4}
0.53	9.89×10^{-3}	0.907	3.6×10^{-4}
0.63	5.88×10^{-3}	0.983	7.5×10^{-4}
0.73	3.48×10^{-3}	1.066	1.0×10^{-3}
0.83	2.05×10^{-3}	1.156	1.9×10^{-3}
0.93	1.21×10^{-3}	1.254	2.4×10^{-3}
1.03	7.06×10^{-4}	1.360	3.0×10^{-3}
1.13	4.11×10^{-4}	1.475	3.7×10^{-3}
1.23	2.39×10^{-4}	1.600	4.6×10^{-3}
1.33	1.39×10^{-4}	1.735	5.6×10^{-3}
1.43	7.99×10^{-5}	1.882	6.9×10^{-3}
1.53	4.60×10^{-5}	2.041	8.5×10^{-3}
1.63	2.64×10^{-5}	2.214	1.0×10^{-3}
1.73	1.51×10^{-5}	2.402	1.3×10^{-3}
1.81	9.66×10^{-6}	2.566	1.7×10^{-3}

E2 Cross-correlating two measurements with different redshift bins

Since the width of redshift bins is generally different for each observation, we perform the following procedure for different width of bins when cross-correlating in Section 4.3.

We have the survey parameters as summarized in Appendix E: the mean redshift $z_i^{\rm X/Y}$, width of redshift bins $\Delta z_i^{\rm X/Y}$, number density $n_i^{\rm X/Y}$, and bias $b_i^{\rm X/Y}$ where the subscript i stands for the ith redshift bin. Then, we define the number density and bias for the survey Y as a function of redshift:

$$n^{\rm Y}(z) = n_i^{\rm Y} \quad \left(z_i^{\rm Y} - \Delta z_i^{\rm Y}/2 \le z \le z_i^{\rm Y} + \Delta z_i^{\rm Y}/2\right), \tag{E2}$$

$$b^{\rm Y}(z) = b_i^{\rm Y} \quad \left(z_i^{\rm Y} - \Delta z_i^{\rm Y}/2 \le z \le z_i^{\rm Y} + \Delta z_i^{\rm Y}/2\right), \tag{E3}$$

where these functions correspond to the plots shown in Fig. 9. Then, we obtain the number density and bias for the survey Y in the mean redshift and redshift bin for the survey X by

$$\tilde{n}_i^{\rm Y} = \frac{1}{\Delta z_i^{\rm X}} \int_{z_i^{\rm X} - \Delta z_i^{\rm X}/2}^{z_i^{\rm X} + \Delta z_i^{\rm X}/2} n^{\rm Y}(z)\,{\rm d}z, \tag{E4}$$

$$\tilde{b}_i^{\rm Y} = \frac{1}{\int_{z_i^{\rm X} - \Delta z_i^{\rm X}/2}^{z_i^{\rm X} + \Delta z_i^{\rm X}/2} n^{\rm Y}(z)\,{\rm d}z} \int_{z_i^{\rm X} - \Delta z_i^{\rm X}/2}^{z_i^{\rm X} + \Delta z_i^{\rm X}/2} b^{\rm Y}(z) n^{\rm Y}(z)\,{\rm d}z. \tag{E5}$$

Thus, we obtain the survey parameters $(b_i^{\rm X}, \tilde{b}_i^{\rm Y}, n_i^{\rm X}, \tilde{n}_i^{\rm Y})$ in the common mean redshifts and redshift bins of the survey X. In this definition, when the mean redshift and redshift bin for the survey

X are the same as ones for the survey Y, we obtain $\tilde{b}^{\rm Y} = b^{\rm Y}$ and $\tilde{n}_i^{\rm Y} = n_i^{\rm Y}$.

APPENDIX F: SIGNAL-TO-NOISE RATIO IN SIMULATIONS: AS A FUNCTION OF HALO MASS

When performing N-body simulations with a halo finder algorithm, we observe all haloes with their masses and number density. In this appendix, assuming the minimum mass $M_{\rm min}$ and the width of logarithmic mass bins $\Delta\ln M$ in simulations, we ideally split two populations:

$$(M_1, M_2, M_3) = (M_{\rm min}, M_{\rm min}e^{\Delta\ln M}, M_{\rm min}e^{2\Delta\ln M}) \tag{F1}$$

and thereby we discuss the signal-to-noise ratio, as a function of $M_{\rm min}$ and $\Delta\ln M$. This investigation provides us with an insight into the detectability in N-body simulations including special and general relativistic effects (Breton et al. 2019; Guandalin et al. 2021).

Using two mass bins, the parameters to evaluate the dipole moment are given by

$$n_{\rm Y} = \int_{\ln M_1}^{\ln M_2} \frac{{\rm d}n}{{\rm d}\ln M}\,{\rm d}\ln M, \tag{F2}$$

$$\langle A_{\rm Y}\rangle = \frac{1}{n_{\rm Y}}\int_{\ln M_1}^{\ln M_2} \frac{{\rm d}n}{{\rm d}\ln M}\,A(M)\,{\rm d}\ln M, \tag{F3}$$

$$n_{\rm X} = \int_{\ln M_2}^{\ln M_3} \frac{{\rm d}n}{{\rm d}\ln M}\,{\rm d}\ln M, \tag{F4}$$

$$\langle A_{\rm X}\rangle = \frac{1}{n_{\rm X}}\int_{\ln M_2}^{\ln M_3} \frac{{\rm d}n}{{\rm d}\ln M}\,A(M)\,{\rm d}\ln M, \tag{F5}$$

where we define $A = M, b_{\rm ST}(z, M)$, and $\phi_{\rm NFW,0}(z, M)$, and the function ${\rm d}n/{\rm d}\ln M$ is the Sheth-Tormen mass function.

Since all the galaxies within haloes would not be detected in real observations, we introduce a suppression factor, the so-called halo occupation number $0 < f_{\rm halo} \leq 1$: the number of galaxies found in a virialized halo of a given mass, in the number density of haloes. Thus this factor can be regarded as a kind of halo occupation number. If $f_{\rm halo} = 1$, all haloes in simulations are assumed

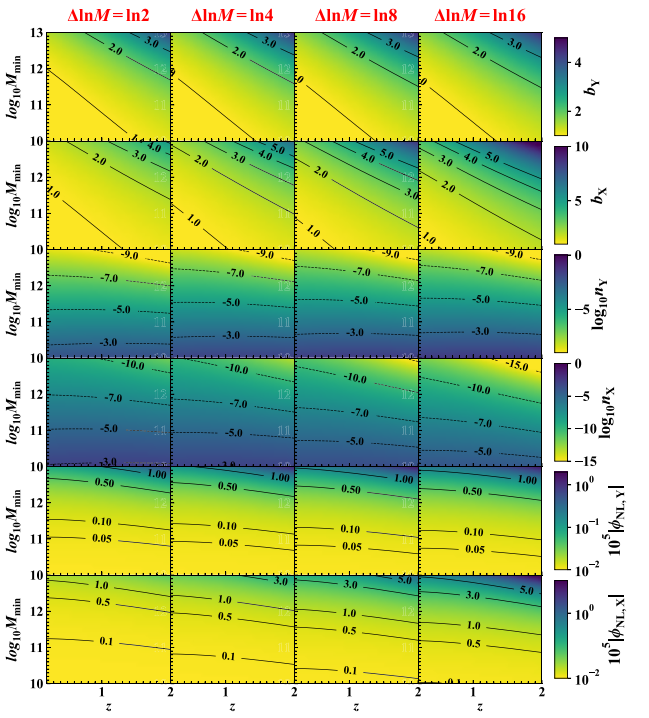

Figure F2. The relevant parameters to compute the signal-to-noise ratio in Fig. F1. From top to bottom, we present the parameters as a function of the mean redshift and minimum mass, $b_{\rm Y}$, $b_{\rm X}$, $n_{\rm Y}$, $n_{\rm X}$, $\phi_{\rm NL\,Y}$, and $\phi_{\rm NL\,X}$, respectively. From left to right, the logarithmic mass bin $\Delta\ln M$ is varied from ln 2 to ln 16.

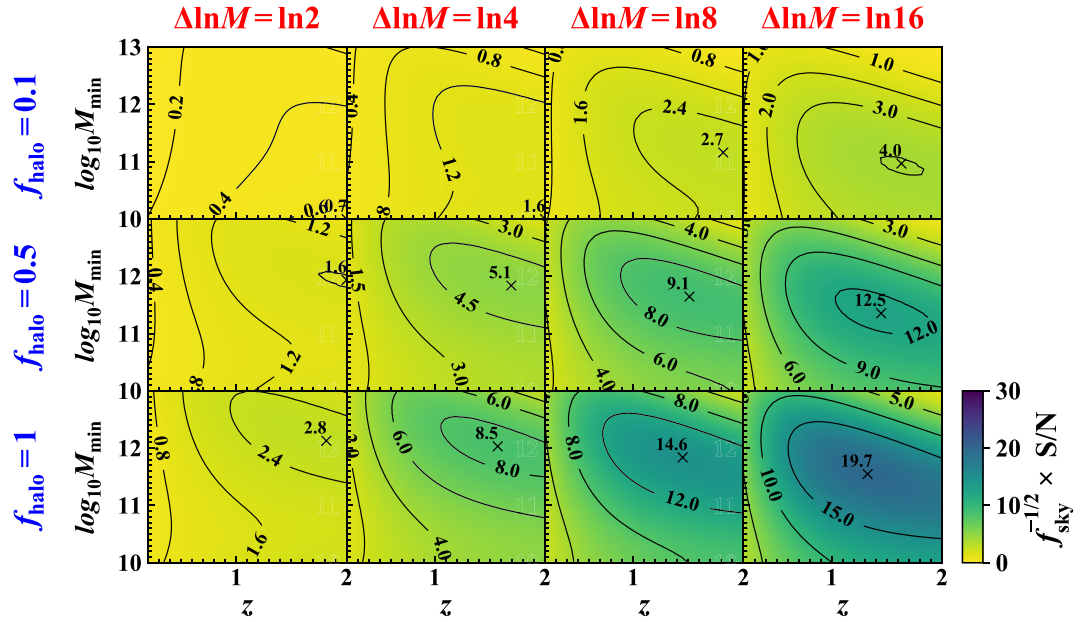

Figure F1. Signal-to-noise ratio as a function of the minimum halo mass $M_{\rm min}$ and mean redshift z. From left to right, the logarithmic mass bin $\Delta\ln M$ is varied from ln 2 to ln 16, and from top to bottom, the parameter $f_{\rm halo}$ is varied from 0.1 to 1. The cross symbols accompanied by a number indicate the parameters that give the maximum signal-to-noise ratio in the parameter space and the corresponding value of the signal-to-noise ratio. The width of the redshift bins is fixed to $\Delta z = 0.1$.

to be detected. In calculating the covariance matrix and signal-to-noise ratio, we multiply this factor by the number density of haloes.

In Fig. F1, we show the signal-to-noise ratio normalized by the fractional sky coverage $f_{\rm sky}$ as a function of the minimum halo mass $M_{\rm min}$ and mean redshift z. This figure indicates that the signal-to-noise ratio becomes maximum at $z \approx 1.3$, slightly depending on the parameters $\Delta \ln M$ and $f_{\rm halo}$. Note that the width of the redshift bins is fixed to $\Delta z = 0.1$ in this figure. This value of redshift at which the signal-to-noise ratio is maximum is different from Figs 7 and 8 because the number density is not constant in Fig. F1, but depends on the redshift following the Sheth-Tormen mass function. In Fig. F2, from top to bottom, we have shown the parameters as a function of the mean redshift and minimum mass, $b_{\rm Y}$, $b_{\rm X}$, $n_{\rm Y}$, $n_{\rm X}$, $\phi_{\rm NL\,Y}$, and $\phi_{\rm NL\,X}$, respectively.

Fig. F1 is useful to discuss the detectability for the dipole moment in simulations. For example, comparing the amplitude of the signal with its error bars in Fig. 2, the signal-to-noise ratio is roughly given by $({\rm S}/{\rm N}) \approx 4$ in simulations with the following parameters: $\Delta \ln M \approx 2$, $\Delta z \approx 0.5$, $M_{\rm min} \approx 2 \times 10^{12}\, M_{\rm sun}\, h^{-1}$, and $f_{\rm sky} = 1$ (see Breton et al. 2019), which lie at the region shown in the bottom-leftmost panel of Fig. F1. Looking particularly at $z \approx 0.3$, we obtain the signal-to-noise ratio of ${\rm S/N} \approx 0.8$ for the width $\Delta z = 0.1$. Accounting further for the width of the redshift bins, a simple multiplication by the factor 5 results in ${\rm S/N} = 4$, which reasonably agrees with the signal-to-noise ratio estimated from the measured dipole amplitudes and their error bars in simulations (Breton et al. 2019; Saga et al. 2020).

This paper has been typeset from a TEX/LATEX file prepared by the author.